ADVANCED OPTICAL MATERIALS
www.advopticalmat.de

Block Copolymer Directed Metamaterials and Metasurfaces for Novel Optical Devices

Alberto Alvarez-Fernandez, Cian Cummins,* Matthias Saba, Ullrich Steiner, Guillaume Fleury, Virginie Ponsinet, and Stefan Guldin*

Optical metamaterials are artificially engineered architectures that exhibit desired optical properties not found in nature. Bespoke design requires the ability to define shape, size, orientation, and composition of material structures on the nanometer length scale. Bottom-up self-assembly methods, such as block copolymer (BCP) templating, offer unique pathways to tailored features, at spatial resolution not routinely achieved by conventional top-down techniques. In this review, the authors provide the general readership with basic concepts of the underlying fabrication processes and examine optical phenomena arising from BCP-derived metamaterials and nanoresonators, with both dielectric and plasmonic characteristics. A number of diverse structural conformations designed by BCP templating and their implementation in optical devices is evaluated. The discussion includes 3D metamaterials, such as gyroidal and hyperbolic arrangements, as well as 2D metasurfaces. Based on recent developments in exploring these emerging structural and material configurations, the review further highlights unexplored opportunities offered by BCP self-assembly for novel metamaterials and metasurface devices.

1. Introduction

Metamaterials are a class of artificial media composites that exhibit on-demand electromagnetic properties, which are not readily observed in nature, e.g., artificial magnetism,[1] negative refractive index,[2–4] epsilon-and-mu-near-zero,[5] light trapping,[6] or low frequency plasmons.[7] Such properties make metamaterials a promising platform to design devices with a wide range of uses for society including super-resolution imaging,[8–10] invisibility cloaking,[11–13] chemical/biomolecular sensing,[14–16] antennas,[17] or absorbers.[18,19] These new functionalities can be achieved by for example using building blocks (so-called meta-atoms) arranged at length scales that are much smaller than the incident wavelength.[20–22]

In this review article, we focus on the engineering of the optical properties for metamaterials active in the visible and near-infrared (IR) wavelength range. Structural features should be on length scales significantly smaller than the visible wavelengths (400–750 nm) to avoid diffractive effects. Material engineering at such length scales is extremely challenging, especially since well-ordered and controllable nanostructures over millimeter-sized areas are required. A variety of different fabrication techniques have been used to produce such structures. Top-down lithographic techniques, such as photolithography, electron-beam lithography, focused ion-beam etching, or nanoimprint lithography provide pathways for the fabrication of complex 2D and 3D metamaterials.[23–29] As a result, a number of high-performance metasurface-based optical devices including flat lenses,[30,31] beam reflectors,[32,33] or meta-deflectors,[34] as well as stacked-planar and chiral 3D structures[35,36] have been demonstrated. However, top-down techniques have a major drawback: the fabrication process is usually nonparallel to traditional manufacturing, making it difficult and time-consuming to precisely control the size, shape, and spacing of the metamaterial features at the nanoscale over large areas. In particular, the fabrication of 3D metallic structures with the required feature sizes below 100 nm represents a scientific challenge for top-down techniques.[22,37] The integration of metamaterial devices that are based on complex, expensive, and non-CMOS compatible techniques is unlikely in the near term. To this end, bottom-up approaches have emerged as possible alternative or complementary platform to top-down techniques.

Bottom-up approaches use chemical or physical forces to spontaneously self-assemble, organize atoms, molecules, or

Dr. A. Alvarez-Fernandez, Dr. S. Guldin
Department of Chemical Engineering
University College London
Torrington Place, London WC1E 7JE, UK
E-mail: alberto.fernandez@ucl.ac.uk
Dr. C. Cummins, Dr. G. Fleury
Centre de Recherche Paul Pascal (CRPP) – UMR 5031
Pessac 33600, France
E-mail: cian.a.cummins@gmail.com
Dr. C. Cummins, Dr. V. Ponsinet
Univ. Bordeaux, CNRS, Bordeaux INP, LCPO – UMR 5629
Pessac 33600, France
Dr. M. Saba, Prof. U. Steiner
Adolphe Merkle Institute
University of Fribourg
Ch. des Verdiers 4, Fribourg 1700, Switzerland
The ORCID identification number(s) for the author(s) of this article can be found under https://doi.org/10.1002/adom.202100175.

DOI: 10.1002/adom.202100175

nanoscale building blocks into larger ordered structures. In contrast to top-down approaches, bottom-up strategies provide simple routes to generate complex features with desired periodicities and can further be combined with other methodologies to grant access to additional structural complexity and control.[38–40] The self-assembly of colloidal particles has proven to be an inexpensive method to fabricate nanoscale structures in 2D and 3D with a wide variety of possible shapes.[41–44] A common route relies on capillary forces to organize colloids during the evaporation of a liquid, leading to the crystallization of spheres into a multilayered 3D face-centered cubic lattice,[45] or their packing into amorphous structures.[46] Colloidal crystals, inverse opals and photonic glasses have been developed using colloidal particles.[47–51] Alternatively, common deposition techniques, such as drop-casting,[52] spin-coating[53,54] or Langmuir–Blodgett[55,56] allow the production of 2D colloidal architectures. In this context, plasmonic colloidal metasurfaces have been widely employed in surface-enhanced Raman spectroscopy (SERS).[57–59] Recently, other methodologies such as the synthesis of patchy particles,[60] or cooperative colloidal self-assembly using DNA[61,62] or viruses[63] have been developed in order to create more complex architectures. Nevertheless, the complexity of materials synthesis and assembly remains significant, limiting their application to-date to small substrates or coupons areas.[64]

In contrast, block copolymer (BCP) self-assembly has emerged over the past decade as a practical approach, offering unrivalled opportunities to design nanometric features with controlled periodicity over extensive areas at low energy and technology cost.[65–67] In particular, the selective hybridization of polymeric domains with inorganic species within BCP thin films has been established as a successful fabrication methodology for visible-range metamaterials.[68–72] The intrinsic BCP phase behavior and opportunities for macromolecular engineering of BCP chains offers a large portfolio of structures and symmetries achievable through BCP self-assembly, making these systems highly promising for optical metamaterials design.[73,74]

Here, we review the latest state-of-the-art progress on BCP-directed 2D and 3D optical metamaterials. We will first provide an overview of the fundamental aspects of optical metamaterials (Section 2), and the impact of global structural arrangement (Section 3), followed by an introduction to BCP self-assembly (Section 4). Next, we will discuss the potential applications of BCP self-assembly based on different 2D and 3D optical metamaterials, including chiral, hyperbolic, and nonlinear 3D optical metamaterials as well as high refractive index and surface-sensitive 2D metasurfaces (Section 5). Finally, we conclude with a brief perspective on the future development of optical metamaterials and metasurfaces based on BCP self-assembly and highlight particular opportunities (Section 6).

2. Optical Metamaterials

In this section, we introduce the fundamental concepts underlying the design and study of optical metamaterials. We first discuss (effective) electro-magnetic parameters that characterize the behavior of a large class of natural materials and metamaterials alike in Section 2.1. In Section 2.2, we elaborate on the role of local resonators, also known as meta-atoms, in metamaterial theory and design. Finally, Section 2.3 introduces the basic properties of percolating metallic metamaterials, such as infinitely long wires or 3D networks.

2.1. From Natural Materials to Metamaterials

The optical properties of a large class of naturally occurring materials can be characterized by a complex refractive index $\overline{n}$ that generally depends on the frequency ν or the wavelength $\lambda = c/\nu$

$$\overline{n}(\lambda) = n(\lambda) + ik(\lambda) \tag{1}$$

The real part $n \in \mathrm{R}$ is also called the optical refractive index and the imaginary part $k \in \mathrm{R}$ is the extinction coefficient.[75]

For most materials, the complex refractive index, which describes wave propagation and refraction, is correlated to the material's intrinsic electromagnetic interaction parameters,[76] the (relative) complex electric permittivity, $\overline{\varepsilon}$, and the (relative) complex magnetic permeability, $\overline{\mu}$

$$\overline{n} = \pm\sqrt{\overline{\varepsilon}(\lambda)\,\overline{\mu}(\lambda)} \tag{2}$$

The branch of the complex square-root (±) is determined by the intrinsic physics of electromagnetic wave propagation in the material. Passive materials can be classified into four different groups as represented in **Figure 1** according to the real parts of their two electromagnetic parameters. The first quadrant (I) represents materials with simultaneously positive permittivity and permeability and includes most dielectric materials, e.g. metal oxides, polymers, or ceramics. The amplitude and phase of an electromagnetic wave propagate in the same direction in these materials and the appropriate sign in Equation (2) is positive. Quadrant II constitutes metals and doped semiconductors that exhibit negative permittivity at frequencies below their material specific plasma frequency, and for most noble metals in the visible range. Quadrant IV describes the behavior of some ferrite materials with negative permeability at microwave frequencies, but are not accessed by any natural material at visible wavelengths. Finally, the quadrant (III) with simultaneously negative permittivity and permeability supports waves, for which energy and phase propagate in opposite directions. As a result, the sign in Equation 2 is negative, leading to negative refraction. Thus, the natural materials (grey part in Figure 1) only span a limited region of the theoretically accessible ε and μ values. In the visible range, natural materials have a permeability close to 1. [77,78] Dielectrics have a positive ε while metals present a negative ε. All the other regions (in blue) correspond to metamaterials. Thus, custom-designed engineering of metamaterials opens new avenues to manipulate light, surpassing natural material constraints.

Negative refraction is only one of the tailored optical properties that can be engineered by metamaterial designs. Others include a bespoke anisotropy, an ε(-and-μ)-near-zero response,[5] as well as strong chiro-optical behavior.[4,7,79] A number of different strategies to achieve these custom-designed properties

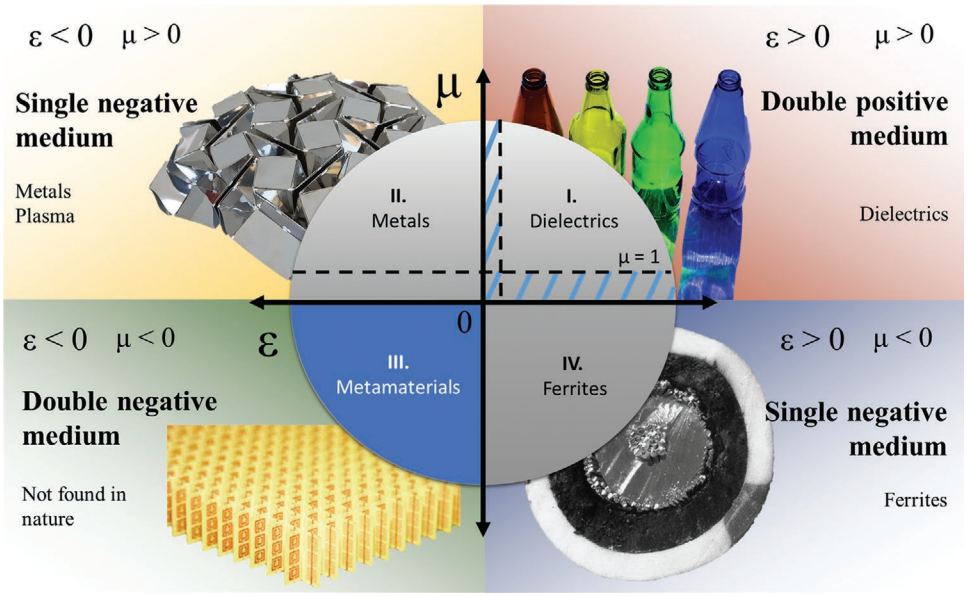

Figure 1. Classification of materials based on the relative electric permittivity ε and relative magnetic permeability μ.

have been proposed over the years. The most well-known and well-studied design principle is based on optical resonators, which will be discussed in Section 2.2. A second important class of metamaterials is fully percolating metallic structures, which are introduced in Section 2.3. Members of this class include so-called hyperbolic metamaterials (Section 5.2), fishnet metamaterials,[80,81] and 3D network metamaterials[82,83] such as the gyroid morphology, which is discussed in Section 5.1.

2.2. Optical Nanoresonators

In the first demonstration of a metamaterial, and in many that followed, the unusual electromagnetic response of metamaterials was created by resonant elements of sub-wavelength size, so-called meta-atoms,[84] with tailor-made shape and organization. Indeed, in their ground-breaking work in 1999, Pendry and co-workers demonstrated that split-ring resonators (SRRs) with dimensions smaller than the excitation wavelength could evoke a magnetic response at the resonant frequency of such an oscillator, even in nonmagnetic parent materials.[76] This proof-of-concept opened the way to design and produce other resonators, including in the nanosize range to target visible wavelengths. When the nanoresonators are produced via top-down methods, the respective features and dimensions are constant in the fabrication process. On the contrary, when they are obtained by bottom-up routes, it is possible to decouple the fabrication and property analysis of the individual meta-atoms from those of the 2D or 3D assemblies. Bottom-up produced meta-atoms are mostly colloidal particles or assemblies of colloidal particles, with feature sizes in the nanorange for visible wavelengths.

Meta-atoms are typically made of either dielectrics of chosen refractive index, or plasmonic metals, exploiting the electromagnetic excitation of their free charge carriers in the conduction band below the plasma frequency, or possibly a combination of both. Resonances in dielectric nanoparticles are based on structural cavity-like Mie-like electric and magnetic multipolar responses. Originating in a cavity effect, Mie-like resonances arise when the light wavelength λ_p inside the particle is commensurate to the size of the dielectric particle (**Figure 2**A). For a dielectric sphere of diameter d, a first dipolar resonance displaying a maximum in the magnetic field inside the sphere is observed for $\lambda_p \approx d$. A second dipolar resonance of electric nature occurs when $\lambda_p \approx d/2$.[85,86] Higher multipolar orders produce resonances at shorter wavelengths but with decreasing strength as the scattering efficiency decreases with multipolar order. Figure 2B shows the electric and magnetic field distribution for the dipolar Mie resonances. At the first dipolar resonance a circular polarization current (Figure 2Bi) generates a magnetic dipole, perpendicular to the incident electric field (Figure 2Bii). Similar field maps are found near the second Mie resonance by switching the roles of the electric and magnetic field. The magnetic and electric Mie resonances can then enhance the local magnetic and electric fields inside the particle at optical frequencies and this enhancement is related to the intrinsic properties of the dielectric particles (Figure 2C).

On the other hand, plasmonic metamaterials are based on metallic meta-atoms where the optical response largely stems from the nontrivial dispersive permittivity of the metal, leading to a localized plasmon resonance.[89] When an oscillating electric field is applied to a metallic nanoparticle, the charge density of the conduction band electrons follows the oscillation of the field, creating electric currents and an effective accumulation of surface charges (**Figure 3**A). This collective behavior can be described using a Lorentzian oscillator, with its resonant peak in the displacement amplitude (or polarizability) at the resonance frequency accompanied by a π phase shift over the spectral width of the resonance (Figure 3B). The fundamental plasmonic mode in a metallic meta-atom is called a localized surface plasmon resonance (LSPR).[89] It produces a considerable enhancement of the electric field in the close vicinity of

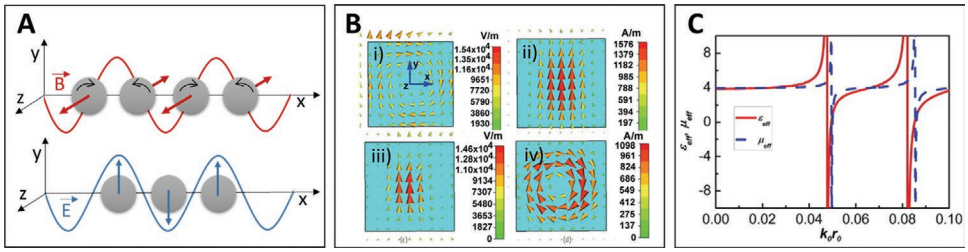

Figure 2. A) The magnetic dipole (top) and electric dipole (bottom) oscillating with the incident electric field of light. B) Electric (left, $z = 0$ plane) and magnetic (right, $y = 0$ plane) field distribution in a dielectric cube near the first Mie resonance (top) and near the second Mie resonance (bottom). Reproduced with permission.[87] Copyright 2008, American Physical Society. C) The effective permittivity ε_{eff} and permeability μ_{eff} of a 3D array of spherical dielectric resonators. Reproduced with permission.[88] Copyright 2013, IEEE.

the particle surface. The field enhancement is at the basis of the SERS effect.[93] The plasmonic modes supported by an individual meta-atom (Figure 3C) are modified by the presence of neighboring particles through plasmon coupling, an effect very similar to the hybridization of atomic orbitals.[94] Plasmonic coupling yields a shift in the LSPR frequency and can strongly increase the field enhancement (Figure 3D). From the point-of-view of the effective metamaterial response, the proximity of the nearest neighbors thus modifies the field distribution around each individual particle. Meta-atoms arranged on a lattice can coherently interact, leading to collective modes if next-nearest neighbor distances are marginally larger than the individual particle size. In analogy to collective particles in solid state physics, such as phonons or electrons, these are best understood in a band structure picture in bulk 3D metamaterials[95–97] and are also known as surface lattice resonances (SLRs) in metasurfaces.[98–100] In summary, the response of plasmonic and dielectric optical metamaterials is not only influenced by the constituent materials and the shape and size of the resonator, but also by the (periodic) arrangement of individual resonators to form a metamaterial.

2.3. Percolating Metallic Structures

Section 2.2 describes how metamaterial properties arise from both the resonant responses of the individual meta-atoms and the interparticle coupling related to the spatial organization of meta-atoms. Optical nanoresonators arranged on a periodic lattice act similar to locally bound electrons in an atomic lattice. Therefore, tuneable individual resonances and hybridization of resonant modes play a dominant role in metamaterials based on meta-atoms. In contrast, electrons in percolating metallic structures are not localized to individual meta-atoms, and the light-matter interaction in this type of metamaterials cannot be understood in terms of elemental response. The nonlocal nature of the plasmonic excitations is best understood in terms of specific bulk modes. Bulk modes are self-consistent light-matter waves, that exist in materials and are characterized by a wave vector $\vec{k}$ and a corresponding frequency dispersion relation $\omega(\vec{k})$. The difference between a metamaterial based on meta-atoms and a percolating network metamaterial is illustrated in **Figure 4**. As mentioned before, most natural materials can be categorized into two classes at optical wavelengths. Dielectric materials follow a linear dispersion relation that emanates from ω and $\vec{k} = 0$ as shown in red and blue in Figure 4A. The associated modes are transverse polarized, either red (right circular polarization) or blue (left polarization) or a superposition of these two, with fields oscillating in the plane perpendicular to the wave vector. Metals, on the other hand, have a plasma frequency, typically in the ultraviolet, below which no propagating modes with considerable lifetimes exist. This is the reason why silver makes a good mirror at optical wavelength. At the plasma frequency, a twofold transverse band emanates

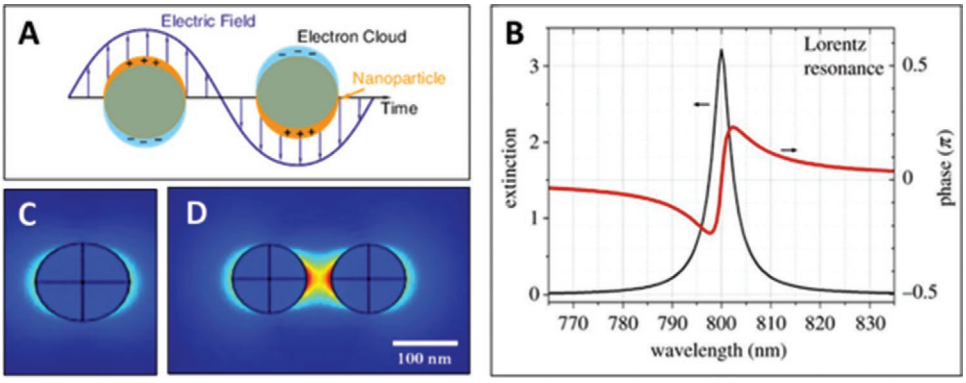

Figure 3. A) Illustration of a localized surface plasmon resonance (LSPR) resulting from the collective oscillations of delocalized electrons in response to an external electric field. Reproduced with permission.[90] Copyright 2015, Springer. B) Extinction and phase of the transmission amplitude through a pure Lorentz resonance. Reproduced with permission.[91] Copyright 2017, The Royal Society. C,D) Simulated electric field distributions (V m^{-1}) of a single gold NP (C) and a dimer (D) illuminated near the plasmon resonance. Reproduced with permission.[92] Copyright 2011, MDPI.

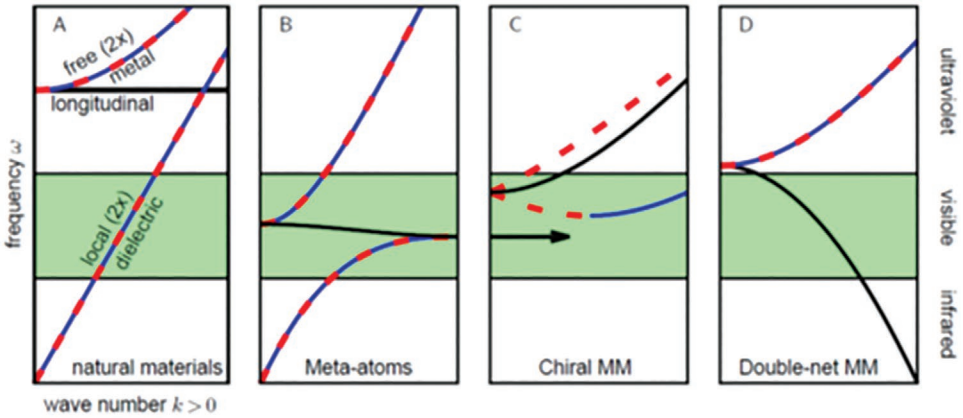

Figure 4. Schematic dispersion relations for different material types: A) Twofold degenerate dielectric dispersion (red and blue), metallic twofold degenerate transverse dispersion, and a flat longitudinal metallic branch (current modulated along the propagation direction, black). B) MM made of isolated meta-atoms. C) MM made of a fully percolating metallic domain. D) A double network MM made of two intertwining metallic domains. The green shaded region highlights the visible frequency domain.

parabolically together with a practically flat longitudinal band (black line), for which the electric field points in the direction of the wave vector. The energy propagation of a particular mode can be correlated to the group velocity, which is the slope of the associated band, while the phase propagation is proportional to the wave vector. Both therefore point in the direction of the wave vector for the transverse modes in natural materials.

The dispersion for a typical monatomic metamaterial based on meta-atoms is illustrated in Figure 4B. The dispersion relation resembles a dielectric material for large parts of the spectrum, except for frequencies close to the meta-atom resonance. A (possibly) negatively sloped longitudinal band exists close to the resonance and leads to counter-propagating phase and group velocity and thus negative refraction (even without obvious magnetic resonances).[96] Due to the fully interconnected nature of percolating network-like metamaterials, these follow a metallic dispersion relation (Figure 4C), but with a reduced electron density and thus a plasma frequency that can be lowered into the optical range. The electron confinement to the network further leads to self-inductance and a dispersive longitudinal band with propagating modes, whose slope can surpass the transverse band for thin networks.[83] Furthermore, percolating chiral metamaterials such as the gyroid (cf. Section 3.1) can cause a considerable splitting of the right and left circularly polarised light[101–103] as a pathway to a chiral route to negative refraction as first established by Pendry.[117]

The resonance-based metamaterial leads to a dispersion relation that resembles that of a dielectric material for frequencies far away from the resonance and can lead to left-handed modes (these have opposing phase and energy velocities) that yield negative refraction. 3D metamaterials based on intertwining double-nets have, on the other hand, recently been shown to possess a (longitudinal and possibly negatively sloped) band between $\omega = 0$ and the materials plasma frequency.[105] This band has already been observed in a double gyroid optical metamaterial in 2011, but not given special attention at the time.[106]

Homogenization strategies[82,102] work well to predict the qualitative behavior of the percolating metamaterial bulk modes, but they fail to model the light-matter interaction close to the surface of the metamaterial, where termination effects can change the metallic network topology and substantially influence the optical properties.[107] Furthermore, homogenized network metamaterials cannot be fully characterized in an effective parameter picture due to the existence of the dispersive longitudinal mode.

2.4. Structural Arrangement in 3D, 2D, and 1D

As discussed in Section 2, the unique electromagnetic response of metamaterials is based on either the presence of optically resonant elements or percolating structures of sub-wavelength size with tailor-made shapes and arrangements. Depending on the dimension of the underlying lattice of such periodic assemblies of plasmonic elements, metamaterials can be classified as 1D metamaterials, 2D metasurfaces, and 3D metamaterials (**Figure 5**).

2.5. 3D Optical Metamaterials

3D metamaterials are designed to monitor light propagation and refraction, controlled by an effective refractive index $\overline{n}$. As was mentioned before, both concepts of elemental resonators and metamaterials assembled therefrom, gained momentum after John Pendry disclosed the split-ring resonator (SRR) design, and it was demonstrated that this design could give access to a negative refractive index material, [109] theorized by Victor Veselago 30 years earlier.[110] Tremendous efforts were subsequently devoted to reaching negative refractive index at optical wavelengths, with the promises of obtaining perfect lenses[10] and invisibility cloaks.[111] However, the resonators produced, by micro- and nanofabrication, along this design and subsequent ones[22] have been mostly inappropriate for the construction of 3D metamaterials, apart from some stacked materials.[26,112] By contrast, resonators produced by bottom-up routes, as colloidal nano-objects, can be assembled by physico-chemical methods.[46,113–115]

Percolating plasmonic structures, and some chiral structures[104] are intrinsically 3D, and affect light propagation in the

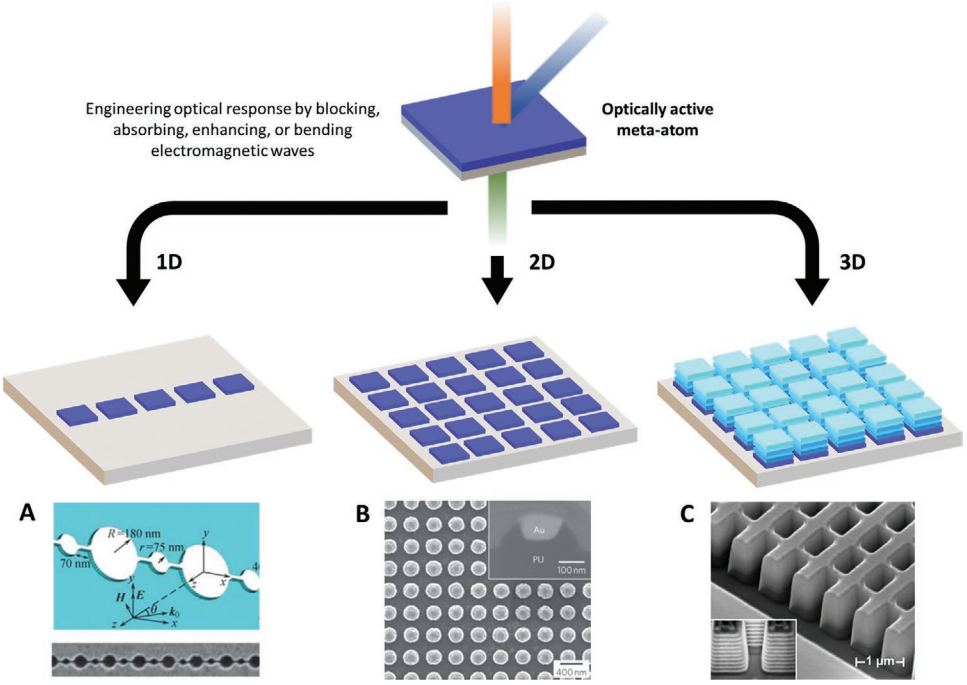

Figure 5. From single meta-atoms to 3D metamaterials: A single nanoresonator is arranged at close proximity with several others to form chains (1D) and a square array (2D). Such structures can be extended to form a 3D material. A) Design (top) and SEM image (bottom) of 1D meta-chains for optical wave-guidance. Reproduced with permission.[90] Copyright 2015, Springer. B) SEM image of a 2D metasurface consisting of gold resonators arranged on a square lattice. Reproduced with permission.[108] Copyright 2011, Springer Nature Limited. C) SEM image of a 3D metamaterial consisting of a double fishnet structure. Reproduced with permission.[26] Copyright 2008, Springer Nature Limited.

material. Interestingly, studies have demonstrated that a strong chirality or anisotropy, in combination with strong resonances, can lead to negative refraction index without necessarily having both negative permittivity and permeability.[104,116,117] Chiral and hyperbolic metamaterials are discussed in more detail in Sections 5.1 and 5.2.

2.6. 2D Optical Metasurfaces

Following the seminal SRR design, more 2D resonator designs were proposed and investigated, downsizing to nanoscales[22] and visible or near-visible wavelengths, including U-shaped,[118] paired nanorods,[3] metal/dielectric/metal fishnet structures,[119] which can efficiently be produced as 2D assemblies.

Metasurfaces are effectively 2D versions of metamaterials, and have attracted considerable attention in the last 10 years.[19,120–122] Their success can be understood through two key advantages. First, metasurfaces are easier to fabricate and thus offer better scalability and lower production cost. Second, in comparison to 3D bulk metamaterials, metasurfaces sub-wavelength thickness minimizes the undesirable optical losses and strong dispersion associated with the resonant responses.[123] Additionally, their nanometer thickness results in a relatively small phase propagation compared to 3D optical metamaterials: while 3D materials affect propagation and refraction, via refractive index engineering, metasurfaces affect reflection and transmission, relying on the responses of the constituting nanoresonators in terms of light scattering.[124] Such nanostructures can resonantly interact with light waves and re-emit it with a controlled phase, modality, polarization, or spectrum.[125] Therefore, abrupt and controllable changes of optical properties can be achieved by engineering the interaction between light and the array of the scattering meta-atoms. In this sense, manufacturing techniques provide a strict control over the structural parameters (e.g., size, shape, and interparticle distance), while enabling a high versatility of material structures. This ability to manipulate light at the nanoscale has opened a plethora of practical applications for 2D optical metasurfaces, including cloaking,[126] metasurface-based absorbers,[127,128] high-refractive index surfaces,[68,72] polarization transformers,[129] wave front engineering[130–132]or wave antennas.[133] Optical metasurfaces are discussed in more detail in Section 5.3.

2.7. 1D Optical Metamaterials

1D metamaterial structures exhibit some of the fundamental properties of their 2D and 3D counterparts.[134,135] Two main types of 1D metamaterials can be distinguished: layered metal-dielectric structures[136] and confined linear chains of meta-atoms, often simply through spheres or disks architectures.[137] The first type makes a hyperbolic metamaterial and will be discussed in detail in Section 5.2. The second type is mainly controlled by the interparticle distance, although the effect of different meta-atom shapes has been studied.[138] The modes of these 1D chain metamaterials can be qualitatively well understood with a simple particle pair interaction model similar to a tight binding approach in condensed matter physics,[139] or in this case particularly a Su-Schrieffer–Heeger model.[140] The

long-range interaction between the underlying plasmonic metaatoms and the associated lattice sums constitute a mathematical rather than a conceptual problem, so that analytical closed form expressions for the material modes of 1D chain metamaterials exist. These materials have thus proven ideal candidates to study advanced applications, such as topological end states[141] and cavity free nanolasing.[142]

2.8. Block-Copolymer Self-Assembly

As introduced in Section 1, optical metamaterials (operating at visible frequencies) require the fabrication of 2D and 3D composite materials designed with sub-100 nm periodicities or characteristic size and nanometer scale resolution. Using top-down methodologies, this is problematic to achieve in terms of fabrication time and cost for 2D structures and is currently not feasible for fully 3D materials. Bottom-up self-assembly has proven to be a practical alternative approach that overcomes these limitations. In this context, BCP self-assembly offers unique opportunities to design nanometric features with controlled periodicities over extended wafer-sized areas. Next, we outline the critical factors to consider for BCP templating for metamaterials and metasurfaces.

2.9. Thermodynamics of BCP Segregation Behavior in the Bulk

A BCP is a macromolecule formed by the covalent bonding between two or more chemically distinct polymer chains (referred to as blocks). Depending on the connectivity between the blocks, various macromolecular architectures have been developed, such as diblock, triblock, star, or graft copolymers (**Figure 6**A).[143] A rich variety of nanostructured materials have been produced by the self-assembly of these particular macromolecules owning to their segregation behavior. As the chemical bond between the blocks prevents separation at the macroscopic scale, the separation appears locally, and the periodic structures formed possess length scales related to the radius of gyration of the polymer chains.[144] BCP pattern features are typically on the sub-50 nm range. Microphase separation occurring in AB diblock BCP systems is largely based on three parameters, the volume fractions of each block (f_A and f_B), the number of repeating units or degree of polymerization, ($N = N_A + N_B$), and the interaction parameter between the repeating units, referred to as the Flory–Huggins parameter (χ_{AB}).[145] The enthalpy changes in the segregation process is largely determined by χ, while the change in entropy mainly depends on the degree of polymerization N. Thereby, the product of the interaction parameter with the overall degree of polymerization, $\chi_{AB}N$, as well as the BCP composition, φ, dictates the phase behavior of BCPs.[143]

Extensive research over the last 50 years led to the definition of the BCP phase diagram for the prediction of the equilibrium phases in the f–$\chi_{AB}N$ representation (Figure 6B). For a symmetric AB diblock ($f_A \approx 0.5$), the system will adopt a lamellar (L) configuration, while increasing f_A results in more curved interfaces in order to minimize interfacial area and lower the total interfacial energy. Thus, for asymmetric diblock copolymers, a sequence of gyroid (G), cylinder (C), and sphere (S)

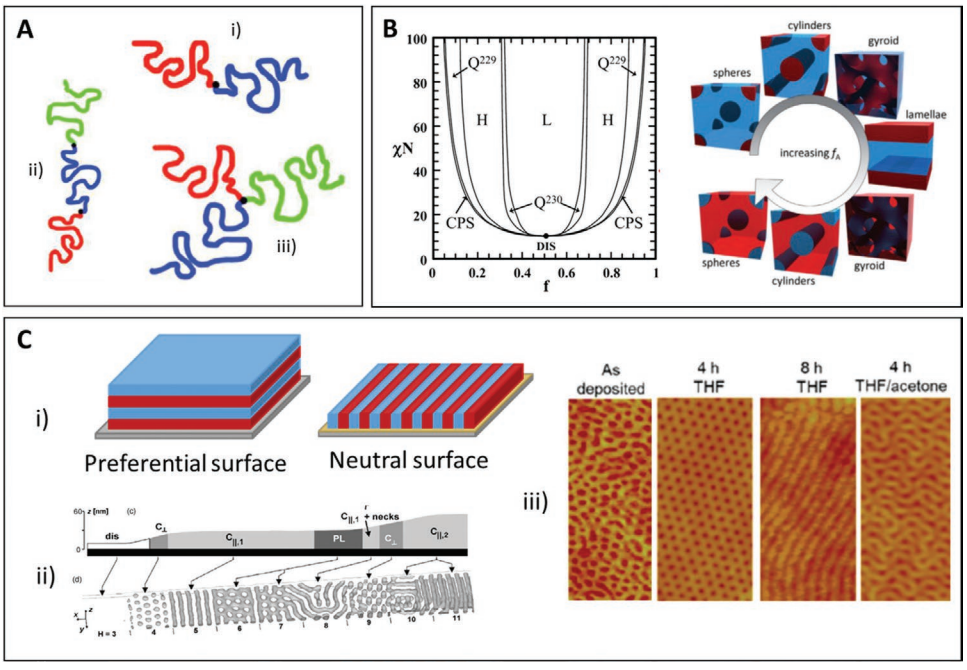

Figure 6. A) Schematics of different BCP configurations: (i) diblock, (ii) triblock, and (iii) miktoarm star BCPs. B) Theoretical phase diagram of AB diblock BCP predicted by the self-consistent mean-field theory (left) and the corresponding morphologies (right). Reproduced with permission.[150] Copyright 2010, Elsevier. C) Additional parameters affecting BCP self-assembly on thin films: i) Effect of the surface fields on the BCP domain orientation, ii) effect of the annealing process. Reproduced with permission.[151] Copyright 2013, American Chemical Society. iii) Effect of the film thickness. Reproduced with permission.[152] Copyright 2002, American Physical Society.

morphologies is found. Increasing the $\chi_{AB}N$ value will further drive the incompatibility between the blocks resulting in a strong segregation regime, with sharp interfaces between the domains.[146] However, significant differences between the above discussed theoretical framework and the experimental phase diagrams have been found.[147] The most important one is the asymmetry with respect to f_A due to the difference of the segment length of the two repeating units, making the prediction of the equilibrium phase diagram more complex.[148,149] Higher-order multiblock BCP have been attracted increasingly attention due to their additional architectural complexity (linear, graft, star, or cyclic), allowing more complex self-assembled structures, expanding the scope of BCP design.[66] Therefore, bulk BCPs constitute a valuable and versatile tool for nanomaterial design, enabling one to access a desired morphology, characteristic size, and physical-chemical functionality by tuning of the chemical nature and the molecular weight of each block.

2.10. From Bulk to Thin Film Configurations

Since BCP-based metamaterials typically involve self-assembly of thin films on substrates, additional parameters (interfacial fields between the BCP domains and the substrate, confinement effects, etc.) have to be considered in order to understand the resulting self-assembled structures.

For example, the control of the interfacial energy between the BCP domains, the substrate and the free surface is critical with regards to the mesostructure stability[153] and orientation.[154] If the interfacial energy field is preferential for one of the blocks, this block domain tends to wet this particular surface and *in-plane* orientations will be preferentially obtained (parallel to the substrate). In contrast, neutral interfaces may favor *out-of-plane* orientation of the mesostructure, depending on the BCP film thickness and its commensurability regarding to the BCP period[155] (see Figure 6C(i)). The most common strategy to modify these interfacial energy fields, and therefore to control the BCP mesostructure orientation, is the use of neutral grafted layers[156] or top-coats,[157] while solvent vapor annealing has also been shown to provide precise control of the structure orientation due to a tuneable affinity between the solvent vapor and the BCP domains[151] (Figure 6C(ii)).

Of equal importance are the confinement effects related to a mismatch between the BCP film thickness and its natural periodicity. This mismatch can induce significant deviations from the predicted bulk structures. As an example, Knoll et al.[152] have demonstrated how various morphologies obtained from a cylindrical BCP could be stabilized as a function of the film thickness. Perforated lamellae, different orientations of the cylindrical structure as well as coexistence between two different morphologies were obtained depending on the commensurability of the inherent BCP phase periodicity and the film thickness (Figure 6C(iii)). For metamaterial design applications, all these parameters are of critical importance as the final response of plasmonic and dielectric optical metamaterials are extremely sensitive to the particular nanostructure morphology and orientation. If properly studied, interfacial fields and commensurability effects therefore bear the opportunity to enrich the BCP phase diagram with complex structures, enabling more intricate patterns to be employed as a template for metamaterial design.

2.11. Inorganic and Metal Incorporation into BCP Films

The electromagnetic response of optical metamaterials is based on the presence of material components with distinct optical contrast. Therefore, strategies to obtain hybrid BCP-inorganic composites or inorganic replicas are required for metamaterial fabrication. Two particular approaches are most widely employed, the coassembly of a guest material during self-assembly and BCP templating.[158–160]

For nanoparticle coassembly, presynthesized particles are incorporated into the BCP structure mostly through their dispersion in the BCP solution before deposition (see **Figure 7**A). The successful coassembly of nanomaterials into polymer matrices is the result of a balance between the polymer conformational entropy, the enthalpy of the insertion into the polymer matrix, and the NP translational entropy.[159] Enthalpic interactions are based on the surface interactions between the particle and polymer blocks, while entropic interactions depend on the relative size of the NPs and the host polymeric domains. A variety of different metallic and nonmetallic NPs has been selectively incorporated into the desired block copolymer domains, controlling NP size and surface chemistry, and length of the BCP chain, respectively.[161–167] Therefore, BCP coassembly emerges as an interesting approach in the design of highly tuneable optical metamaterial, taking advantage of the possibility of controlling the concentration and size of guest-NPs in the final material (see Section 5.3.1). However, segregation problems at high NP loading or large NPs size can limit the applicability of BCP coassembly in some scenarios, e.g., when highly ordered structures or big (>50 nm) objects are required.

In this sense, templating techniques offer an alternative method to circumvent previously mentioned limitations. Contrary to coassembly approaches, they utilize nanostructured BCP films as scaffolds for inorganic nanofeature fabrication. For example, sequential infiltration synthesis (SIS) is a versatile and straightforward approach for the fabrication of periodic structures via BCP templating.[170–172] SIS is based on atomic layer deposition (ALD) and relies on the alternating pulsing of precursor and reactant gases, separated by purge steps, for depositing thin films. In the case of SIS, selective interactions between the infiltrated vapor-phase precursors and specific BCP domains are used to control the growth of the corresponding inorganic materials.[173] A final etching step to remove the BCP scaffold leads to the formation of the inorganic patterns. High refractive index dielectrics nanostructures, e.g., Al_2O_3, TiO_2, and SiO_2 have been obtained following this approach.[160,174,175] Another route for the metal inclusion into polymer films, directly related to the SIS methodology, is the aqueous metal reduction (AMR) technique. AMR is directed by the selective chemical interactions between one of the BCP domains and the metal ions present in the aqueous solution. O_2 plasma, thermal annealing, UV/ozone or chemical reducing agents were proven to allow reducing the metal ions (see Figure 7B).[176–178] Several protocols have been developed in order to obtain highly defined

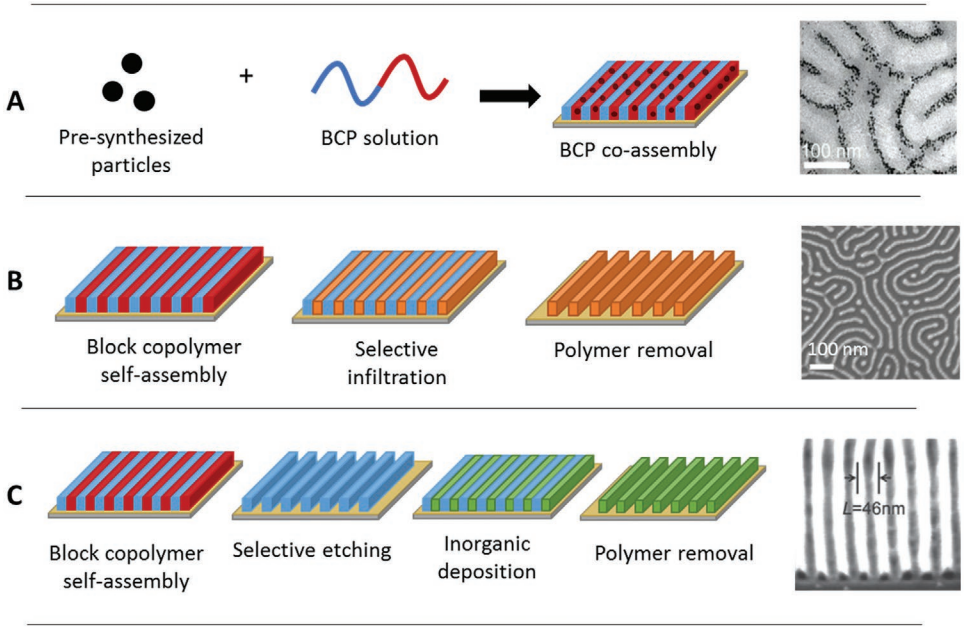

Figure 7. Schematics of the different strategies followed to design optical metamaterials architectures using BCP films as a template: A) BCP coassembly. Reproduced with permission.[169] Copyright 2008, Wiley-VCH. B) Selective infiltration. Reproduced with permission.[68] Copyright 2019, Royal Society of Chemistry. C) Inorganic deposition. Reproduced with permission.[169] Copyright 2014, Wiley-VCH.

Au, Pd, and Pt nanostructures, or even more complex systems like Pt-Au binary NPs following this approach.[179,180] Dielectric materials such as Fe_2O_3, TiO_2, or CuO can be created following a similar methodology, based on the selective inclusion of metallic salts in the BCP films.[181]

Another common templating strategy for nanostructured metals by BCP self-assembly consists of selectively etching one of blocks after phase separation, followed by, electroplating or sputtering a metal through the previously created BCP porous template in order to define geometrical features with defined periodicity.[168,182–184] A final step consisting in the removal of the BCP template is often applied to obtain a free-standing metal replica (see Figure 7C). The ease of processing, the versatility of material inclusion methods, and the overall low-cost make BCP phases ideal candidates for highly scalable processes required for the fabrication of optical devices.[185] The different strategies for inorganic or metallic incorporation into BCP films and the different materials created by the respective techniques are summarized in **Table 1**.

Table 1. Summary of the different strategies for inorganic or metallic incorporation into BCP films.

Strategy	Technique	Inorganic material
BCP coassembly	—	Au,[161–164] Pt,[165] FePt,[166] TiO_2[167]
BCP templating	Sequential infiltration synthesis (SIS)	Al_2O_3,[152] TiO_2,[160] SiO_2[161]
	Aqueous metal reduction (AMR)	Au,[68,180,186,187] Pd,[180,187] Pt[180,187]
	Metallic salt inclusion (MSI)	Fe_2O_3,[181,188] TiO_2,[189] CuO,[181] Al_2O_3[190]
	Evaporation/Sputtering	Cr,[183] Co,[191] Au,[192] Ag[193]
	Electrochemical deposition	Au,[69,101,194] Ag[195]

2.12. Metamaterials Based on BCP Self-Assembly

This section provides an overview of different metamaterial architectures that have been fabricated through metamaterial self-assembly, from fully 3D network-like metamaterials (Section 5.1), over hyperbolic metamaterials (Section 5.2), to 2D metasurfaces (Section 5.3).

3. 3D Gyroid Metamaterials

In the early 2010's, several theoretical studies showed the potential of BCP nanocomposites with so-called single and double gyroid morphologies to obtain 3D metamaterials at visible wavelengths.[196–198] The oriented gyroid is a chiral cubic (specifically space group 214 or $I4_132$ in Hermann–Mauguin notation)[199] triply-periodic minimal surface.[200] In other words, the gyroid has crystallographic cubic symmetry and forms a closed surface subdividing space into two intertwining 3D domains that have the topology of two enantiomorphic chemical $SrSi_2$ (SRS) networks (aka Laves graph).[201] While originally referring to the minimal surface with zero mean curvature everywhere that separates space into two equal volumes, the term gyroid refers in the modern definition to the family of constant mean curvature (CMC) surfaces that minimize their surface area while enclosing an SRS domain with varying spatial fill fraction.[202] In the BCP and optics communities, the term single gyroid refers to this SRS material domain that is bounded by a CMC gyroid. A single gyroid with 20% volume fill fraction

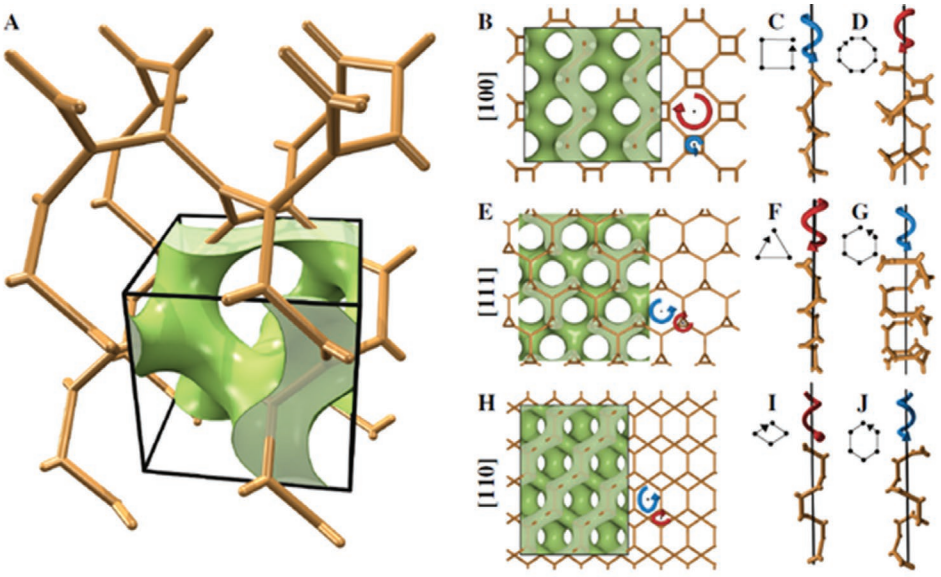

Figure 8. The single gyroid morphology at 20% volume fill fraction (green) and its underlying srs network (brown). A) Perspective view of a single cubic unit cell. B,E,H) Projections onto the fundamental crystallographic directions (smallest Miller indices). Chiral right-handed (red) and left-handed (blue) helical elements of the srs are highlighted with curved arrows. The small elements are shown from the side in C,F,I) and the large elements with opposite handedness in D,G,J). Reproduced with permission.[203] Copyright 2014, The Authors, published by Elsevier.

is illustrated alongside its underlying srs net in **Figure 8**. This figure emphasizes the helical elements that can be found in the chiral structure along different crystallographic directions. The term double gyroid refers to the pair of intertwining single gyroids, each terminated by a CMC gyroid of opposite mean curvature. A double gyroid made of two enantiomorphic network domains (that is with equal volume fill fraction and filled with the same material) is achiral by definition and has cubic symmetry $Ia\bar{3}d$ (space-group 230).

Experimentally, the manufacture of self-assembled gyroid metamaterials commences by the casting of a BCP solution onto a transparent conducting substrate, typically indium-tin-oxide and fluorine-doped tin oxide. After annealing the cast films by heating or in a solvent vapor, allowing the formation of large self-assembled domains, the minority phase (single or double gyroid) is removed by a suitable etching protocol followed by electrochemically backfilling a plasmonic metal, i.e., gold or silver.[70] If required, the remaining polymer can be removed, by thermal degradation or plasma etching. Silver metamaterials are challenging because of the environmental "tarnishing" of silver, but a protocol enabling silver optical metamaterials was recently established.[195]

Both the single and the double gyroid have been investigated as promising candidates to generate a 3D isotropic negative refractive index material. The mechanism behind negative refraction is, however, different in both cases and cannot be understood in the negative homogenized permittivity and permeability picture discussed in Section 2.1. In the case of the single gyroid, negative refraction is based on a separation of the twofold degenerate fundamental plasmonic modes through the inherent chirality of the morphology (Section 2.3). As a result, there is a small frequency region, in which the group velocity points in the opposite direction as the phase velocity, naturally leading to negative refraction.[197] The effect is, however, weakened substantially by the interconnected topology of the gyroid network that prohibits chiro-optical excitation of individual metallic helical elements that has been the underlying assumption in theoretical models. [102] While the material chirality is strong enough to yield substantial circular dichroism,[79] the chiro-optical band splitting (cf. Figure 4C) is negligible at the plasma frequency and, as a result, no evidence of negative refraction has been reported in single gyroid metamaterials to date. Single gyroid metamaterials are nevertheless unique from a fundamental perspective as a template for fully connected, percolating optical metamaterials that cannot be disassembled into meta-atoms. The gyroid is indeed established as a versatile photonic material,[204] both in vitro [205,206] and in vivo,[203,207] with derived chiro-optical multiple gyroid morphologies proposed[207,208] and realized.[209,210] For the single gyroid metamaterial, a number of theoretical and experimental investigations have demonstrated various exotic material properties, such as full tunability of the material response,[102] ultrafast nonlinear effects,[211] and more recently a strong linear[212] and circular[213] dichroism.

The double gyroid has not received the same amount of attention conceivably due to its inherent lack of chirality. In 2011, Hur et al. fabricated a double gyroid metamaterial, and suggested it as an isotropic 3D negative refractive index material.[214] This conclusion was, however, based on a bandstructure calculation in a nonprimitive unit cell, leading to backfolding of the photonic bands into an artificial Brillouin zone and an ostensible negative band slope not connected to left-handed propagation (counter-propagating energy and phase of the associated modes) as required for negative refraction (cf. Section 2.3). Although the double gyroid does not support negative refraction in its fundamental bands, plasmonic double-networks generally hold the promise of yet another intricate mechanism by which 3D isotropic negative refraction

can be achieved that has been overlooked until recently.[215] The required property to exploit this mechanism is an interchange of the two networks upon a primitive lattice translation, implying that the two networks need to be identical (not enantiomorphic). Promising candidates with this property are the double diamond and the plumber's nightmare structures.[216] The extension to single and double diamond morphologies may be feasible but is much more challenging than the gyroid. As pointed out theoretically,[217] increasing the number of strut of the network vertices from 3 (gyroid) to 4 (diamond) increases the local deformation on the copolymer blocks at these vertices, thermodynamically disfavoring diamond over gyroid morphologies. This can be circumvented by adding low concentrations of homopolymer into the blend, which by segregating to the vertices relieve some of these stresses, enabling the self-assembly of diamond morphologies.[218] While demonstrated in the bulk, the formation of well-ordered double diamond morphologies in thins films and their replication into plasmonic metals remains to be demonstrated. Following the above considerations, plumber's nightmare structures with sixfold interconnected vertices are yet more challenging and have not yet been reported in pure polymer systems, but only in more complex material systems.[219]

3.1. Hyperbolic Metamaterials Based on BCP Self-Assembly

In the case of the in-plane lamellar structure, the structural anisotropy of the metallic-dielectric layer stack formed from the two BCP domains, induces an extreme optical anisotropy leading to a so-called *hyperbolic* light propagation,[220–222] Hyperbolic metamaterials represent the ultraanisotropic limit of traditional uniaxial crystals and are often composed of multilayered metal-dielectric nanostacks, or sometimes cylindrical nanocomposites.[223] In such uniaxial metamaterials, one of the principal components of their permittivity tensor ε is opposite in sign to the other two principal components.[224–226] In short, they are materials which behave like a metal in one or two directions of field polarization ($\varepsilon < 0$) and like a dielectric ($\varepsilon > 0$) in the orthogonal directions. The resulting light propagation properties can be used in various applications, such as negative refraction,[227,228] super-resolution imaging,[229] or biosensing.[230]

Basic electromagnetic properties of hyperbolic metamaterials may be understood by considering a nonmagnetic uniaxial anisotropic material with principal axes (x,y,z) and a permittivity tensor

$$\varepsilon = \begin{pmatrix} \varepsilon_1 & 0 & 0 \\ 0 & \varepsilon_1 & 0 \\ 0 & 0 & \varepsilon_2 \end{pmatrix} \tag{3}$$

The iso-frequency dispersion relation in these materials, characterizing the wave propagation, is given by

$$\left(k_x^2 + k_y^2 + k_z^2 - \varepsilon_1 \frac{1}{c^2}\omega^2\right)\left(\left(k_x^2 + k_y^2\right)\varepsilon_1 + k_z^2\varepsilon_2 - \varepsilon_2\varepsilon_1 \frac{1}{c^2}\omega^2\right) = 0 \tag{4}$$

where k_x, k_y, and k_z are respectively the x, y, and z components of the wave vector and ω is the wave frequency. The solution of Maxwell's equations in these homogenized, uniaxial materials admits the characterization of waves (normal modes) with a wave vector $\boldsymbol{k}$, and TE (E-field perpendicular to $\boldsymbol{k}$ and $\boldsymbol{z}$) or TM (E-field in the $\boldsymbol{k}$-$\boldsymbol{z}$-plane) polarization

$$\frac{\omega^2}{c^2} = \frac{\mathbf{k}^2}{\varepsilon_1} \quad \text{(TE)} \tag{5}$$

$$\frac{\omega^2}{c^2} = \frac{\left(k_x^2 + k_y^2\right)}{\varepsilon_2} + \frac{k_z^2}{\varepsilon_1} \quad \text{(TM)} \tag{6}$$

The corresponding dispersion relations define isofrequency contours in $\boldsymbol{k}$-space. The TE waves that only probe the in-plane permittivity of the material are always characterized by spherical isofrequency surfaces (Equation (4)). TM waves on the other hand give rise to ellipsoidal isofrequency surfaces in natural materials where the sign of ε_1 matches that of ε_2 (Equation (5)). On the contrary, in hyperbolic metamaterials, the anisotropy is very strong and the two components ε_1 and ε_2 possess opposite signs ($\varepsilon_1\varepsilon_2 < 0$). Two possibilities then exist: If $\varepsilon_1 > 0$ and $\varepsilon_2 < 0$, the hyperbolic medium is called dielectric hyperbolic or Type I hyperbolic. If $\varepsilon_1 < 0$ and $\varepsilon_2 > 0$, the hyperbolic medium is called metallic or Type II hyperbolic[231,232] (see **Figure 9**A). BCP self-assembly has been revealed as a promising strategy to obtain large scale 3D multilayered materials.[233–235] In this sense, Wang et al.[226] have recently demonstrated for the first time the possibility of using lamellar polystyrene-*block*-poly-2-vinylpyridine (PS-*b*-P2VP) BCP for the fabrication of bulk hyperbolic materials. The PS-*b*-P2VP lamellar phase consists in in-plane alternated PS and P2VP layers (see Figure 9B). When the film was dipped first in a $HAuCl_4$ solution and then in a reducing agent ($NaBH_4$) solution, gold NPs were formed selectively within the P2VP layers. This selectivity is due to the strong affinity between the P2VP domains and the gold precursors. The final structure consists of alternating pure PS and gold NP:P2VP layers (Figure 9B), where the gold NPs are spheres of mean diameter 7 nm, and present a LSPR. Variable-angle spectroscopic ellipsometry and theoretical models were used to extract the permittivity tensor. The obtained results show the possibility to obtain a type II hyperbolic effective medium in a given region of the visible spectrum ($520 < \lambda < 560$ nm) for inserted gold volume fraction larger than 20% (see Figure 9C).

3.2. 2D Metasurfaces

As introduced in Section 3, metasurfaces are 2D versions of metamaterials, in which the optical response is controlled by the presence of sub-wavelength resonant scattering arrays that are custom designed to generate specific optical properties. Therefore, methodologies that allow the design of well-ordered and controllable nanostructures are required. This section reviews the remarkable efforts made to develop BCP self-assembly as a valid and straightforward approach in the fabrication of on-demand metasurfaces.

It is important to note that as for most nanostructures, accessing a precise structural description may be challenging.

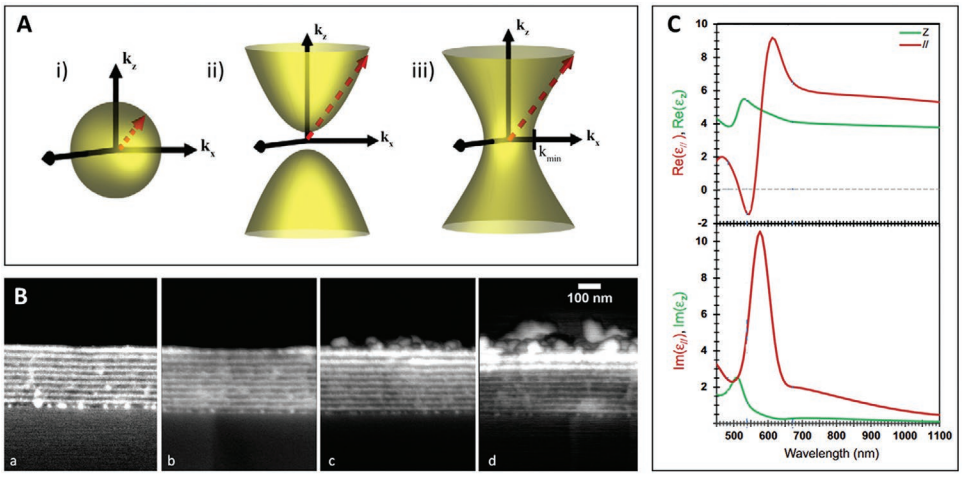

Figure 9. A) Schematic of an isofrequency contour for: (i) an isotropic dielectric, (ii) a type I ($\varepsilon_1 > 0$ and $\varepsilon_2 < 0$), and (iii) a type II metamaterial ($\varepsilon_1 < 0$ and $\varepsilon_2 > 0$). Reproduced with permission.[231] Copyright 2012, IOP Publishing. B) Backscattering scanning electron microscopy side-view image (SEM) of the 265 nm thick film of alternating layers of pure polymer (PS, appearing black) and of gold NPs:P2VP nanocomposite, appearing white, for a number of cycles of gold impregnation and reduction of 5 (a), 10 (b), 20 (c), 30 (d). C) Parallel in-plane (red line) and perpendicular (green line) components of the uniaxial permittivity tensor of the lamellar nanoplasmonic stack. Reproduced with permission.[226] Copyright 2016, Elsevier.

Nevertheless, an accurate description over the structural parameters of the metasurfaces can be invaluable for the understanding of the structure-property relation. Traditional methods of examining nanoscale surface morphologies, such as atomic force microscopy (AFM) or scanning electron microscopy (SEM), are usually insufficient for a full characterization of a thin nanostructure on a substrate. Therefore, other techniques, such as X-ray scattering in reflectivity geometry or ellipsometry can be used, provided appropriate models are available. In particular, both the morphology and the refractive index or the dielectric function of a metasurface can be extracted from ellipsometric data.[236,237] Modeling the optical properties of metasurfaces can sometimes rely on effective-medium theories.[238] In these approaches, the structure is homogenized and an effective permittivity and permeability of the metasurfaces are determined by averaging the electric and magnetic fields over a given thickness. A much used effective medium law is the Maxwell Garnett formula,[239] which has been formulated for dilute spherical inclusions. In order to expand its application to meta-atoms of other shapes, the Maxwell Garnett formula has been modified to ordered and disordered ellipsoids.[240,241] However, for very small thicknesses, the effective index may not be measured independently of the thickness, the measurements conditions or the asymmetry due to the presence of the substrate, which the Bedeaux–Vlieger formalism was developed to deal with.[242] More recently, more complex models dedicated to the characterization of more intricate arrays have been proposed.[243–245]

3.3. BCP Hybrid Thin Film Metasurfaces

During the last few years, various methodologies to use self-assembled BCP thin films to organize plasmonic nanoparticles (NPs) have been disclosed. Different parameters such as the NP size, shape, concentration, surface chemistry, or the BCP length scales and architectures have a significant influence in the distribution of these NPs inside or above the polymer thin film.[246–248] For example, Li and co-workers[163] have shown the possibility to functionalize BCP structures with gold NPs for a polystyrene-*block*-poly-2-vinylpyridine (PS-*b*-P2VP) system (**Figure 10**A). Similarly, Lamarre et al.[161,162] have successfully used this strategy to organize gold NPs in colloidal solutions. Gold NPs were dispersed in a chloroform polystyrene-block-poly(methyl methacrylate) (PS-*b*-PMMA) solution and then spread at the air–water interface in a Langmuir–Blodgett set-up. Based on the higher affinity of water for PMMA, a PMMA thin film on the water surface decorated with PS islands was obtained. Depending on the ligand and size of the particles, the gold NPs were located in the PS part or at the air/PS/PMMA contact line leading to the formation of nanorings. These features were subsequently transferred onto a solid substrate and their optical properties were evaluated. Interestingly, extinction spectra of the gold NPs organized into rings exhibit features of both individual gold NPs and plasmonic rings (Figure 10B). Therefore, by adjusting the diameter of the rings it is possible to tune the optical resonances of the obtained plasmonic structures, from visible to near IR spectrum, or even design devices with multiple resonances in the visible-IR.[161]

Such a strategy is normally limited to small nanoparticles, as larger particles can disrupt the BCP structure, limiting the density of incorporated NPs and therefore the applicability of the obtained structures.[246,248] This restriction can be addressed by the in situ formation of the nanoparticles inside of the BCP matrices.[249] Different methodologies have been used for the reduction of the metallic precursors that were selectively incorporated into the BCP films, leading to the formation of NPs. Recently, Aubrit and co-workers have presented an interesting methodology for the in situ formation of gold NPs in the BCP domains by sonication or radiolysis of the hybrid solutions.[164] This strategy avoids adding extra-species, such as a ligand or chemical reducing agents, leading to the formation of hybrid films of PS-*b*-PVP BCPs containing a dense population of gold NPs organized within oriented cylinders (Figure 10C). The

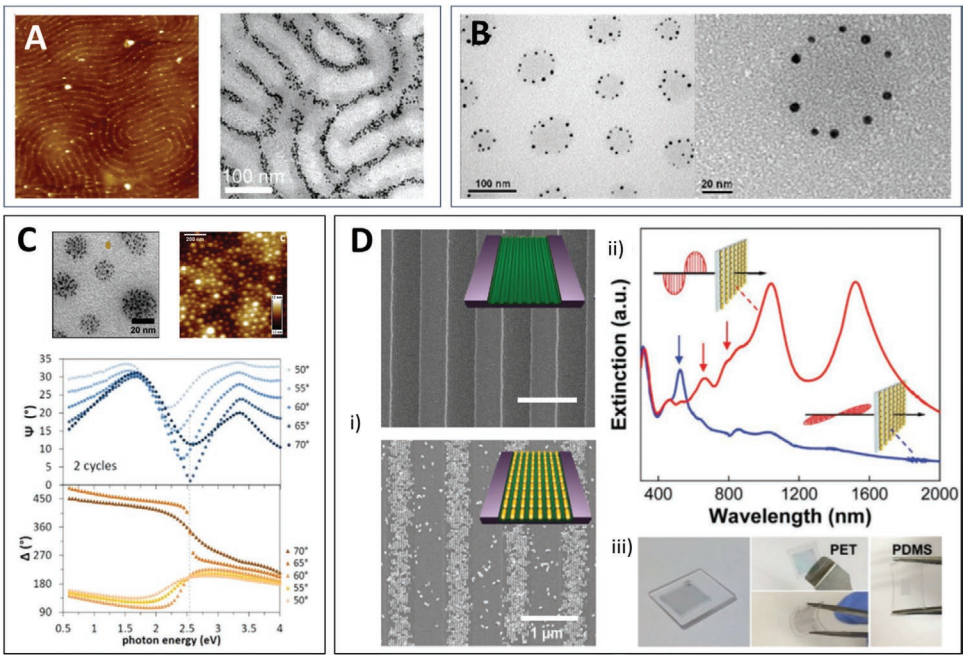

Figure 10. A) AFM (left) and TEM (right) images of PS-*b*-P2VP/gold nanoparticle hybrid thin films. Particles are located at P2VP domains through the control of their surface chemistry. Reproduced with permission.[163] Copyright 2008, Wiley-VCH. B) TEM of the gold nanoparticles forming rings at the interface between the PS domains and the PMMA matrix. Reproduced with permission.[167] Copyright 2013, American Chemical Society. C) AFM and TEM images of the PVP domain containing gold nanoparticles formed by sonication (top) and ellipsometric angles as a function of photon energy for different angles of incidence for the film obtained. Reproduced with permission.[164] Copyright 2018, Royal Society of Chemistry. D) (i) SEM image of linearly aligned grooves of plasma-treated PS-*b*-PMMA thin film on the lithographic pattern (top) and gold NRs deposited on the aligned grooves (bottom). (ii) Polarization-dependent extinction spectra of aligned gold NRs on quartz substrate. (iii) Photos of transferred gold NRs to various substrates. Reproduced with permission.[253] Copyright 2019, Wiley-VCH.

optical characterization of the obtained thin film by ellipsometry showed the existence of a maximum of the ellipsometric angle Ψ at 90°, while the ellipsometric phase angle Δ jumps abruptly by more than 180° (Figure 10C). This behavior called "plasmon-induced Brewster" extinction (or topological darkness)[250] has been observed in other polymer plasmonic nanocomposites[251] and has been identified as a method to enhance sensitivity in plasmonic chemical/biological sensing.[251,252] Another approach to introduce large particles without disrupting the BCP structure has been introduced by Liu and co-workers.[254] In their work, gold nanorods (NRs) were deposited into the nanoscale grooves generated by selective removal of one of the BCP domains. However, the azimuthal degeneracy of the orientation of the BCP system, limited the optical properties of the final structure.[255] Following this idea, and using lithographic patterned substrates, single orientation dichroic structures have been recently presented by Kang and co-workers:[253] directed self-assembly of PS-*b*-PMMA copolymers on lithographic Si patterns allowed a uniform control over the gold NR orientation (Figure 10D). Such dichroic plasmon superstructures offer interesting opportunities for novel optical systems, e.g., waveguides[256] or imaging devices.[257]

3.4. Tuneable Refractive Index Metal Metasurfaces

Other strategies rely on the selective hybridization by metal or dielectric precursors of self-assembled BCP films to produce 2D arrays of nanoparticles. Unlike the strategy presented before, the template polymer film is degraded at the end of the process leading to pure inorganic or metallic arrays on top of the substrate surface. The structural design of the metasurface can be controlled by engineering the macromolecular characteristics of the BCP (defining the morphology and characteristic size of the pattern) and the process used to produce the templating thin film (defining the orientation homogeneity of the pattern). In particular, the molecular weight and the composition of the BCP determine both the interparticle distance and the size of the meta-atom. Both parameters are essential for controlling the metasurface optical response.[258]

Going beyond the physical limit attainable with natural materials is the purpose of the design of metamaterials. As discussed in Section 2, the experimental realization of a negative refractive index has been one of the main focuses in this field. But it is important to note that the value of the refractive index is also limited in the positive regime.[259] Very few natural transparent materials have an index above 2–3 for visible wavelengths.[260] Thus, the realization and the modification on demand of the refractive index towards high positive values constitutes an important step in the implementation of metasurfaces on optical devices ranging from optoelectronics to photolithography.[259] Additionally, simultaneously high refractive index and extinction coefficient materials have been employed in the design of ultrafast all-optical switches due to their maximize absorption of light.[261]

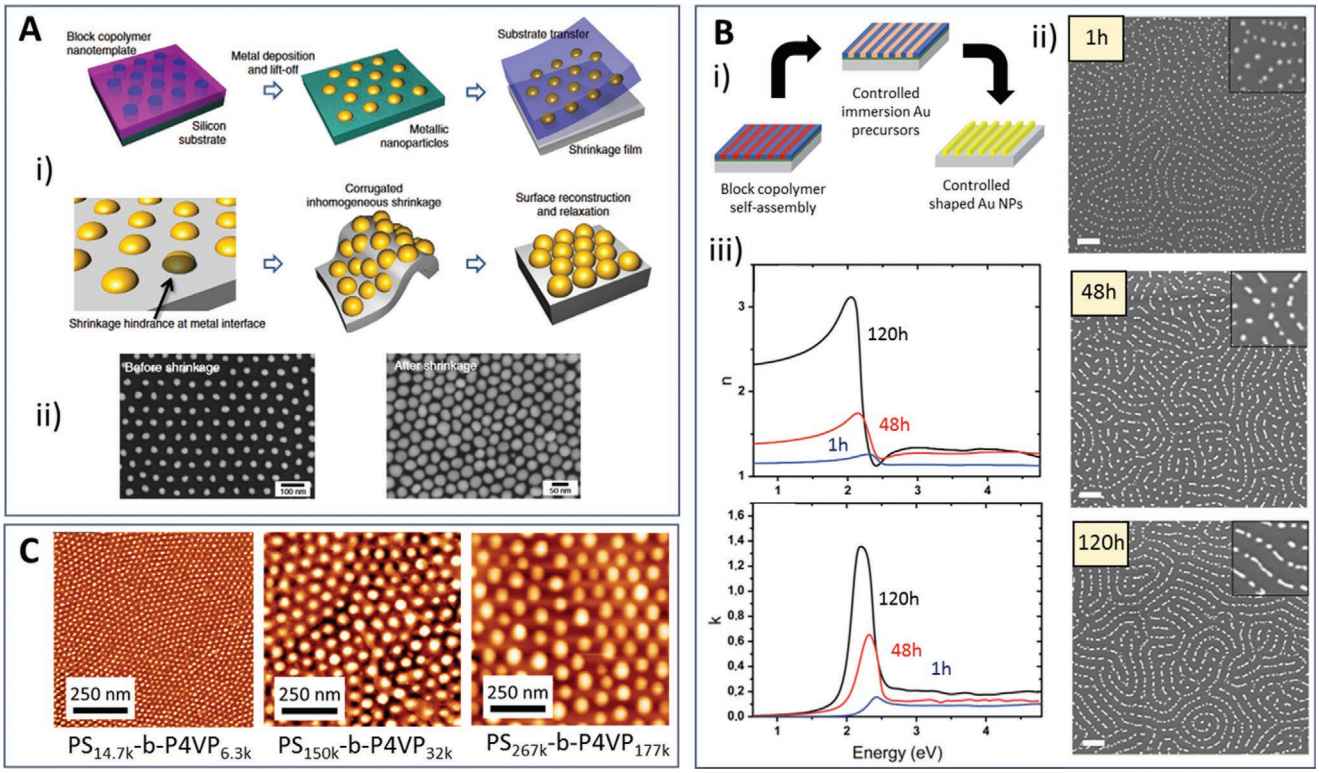

Figure 11. A) (i) Schematic for metal NP metasurface preparation by BCP self-assembly. (ii) SEM images of hexagonal gold NP arrays as-prepared from BCP self-assembly (left) and after complete pattern shrinkage (right). Reproduced with permission.[72] Copyright 2016, Springer Nature. B) (i) schematic illustration of the fabrication of the gold decorated surfaces derived from nanostructured BCP thin films. (ii) SEM images of discreet gold nanoparticle arrays formed on a silicon substrate using a PS-*b*-P2VP BCP template by immersion in aqueous gold precursor solution for different times. (iii) Refractive index of the studied nanostructured surfaces. Reproduced with permission.[240] Copyright 2019, Royal Society of Chemistry. C) AFM topographical images of the three sizes gold NP hexagonal arrays obtained using three different molecular weight BCP as template. Reproduced with permission.[243] Copyright 2020, AIP Publishing.

In 2016, Kim et al.[72] demonstrated the potential of BCP thin film templating for the design of bespoke metasurfaces. Tailored optical properties were obtained by controlling the structural parameters of the plasmonic array. Thereby, high and tuneable refractive index materials were obtained by modifying the interobject distance in the plasmonic array. In particular, PS-*b*-PMMA films with out-of-plane hexagonal cylindrical packing were created on silicon substrates (**Figure 11**A). After etching of the PMMA domains by immersion in acetic acid and UV exposure, hexagonal gold nanodots were obtained by e-beam evaporation onto the PS porous film. To modify the interparticle distance, the gold structure was transferred onto a PMMA substrate by a lift-off process, and then deposited onto a polydimethylsiloxane (PDMS) stamp allowing a shrinkage of the interobject distance through thermal annealing. A heat treatment at 180 °C for 3 min promoted a lateral film shrinkage of 40%, with a subsequent decrease of the interobject distance from 33 to 2.8 nm. The precise manipulation of the interobject distance allowed to increase the refractive index of such metasurfaces from around 1 to 5.1. More recently, Alvarez–Fernandez and co-workers presented another fabrication technique of high-refractive index surfaces by controlling the meta-atom shape.[68] The selective and controllable hybridization of the out-of-plane lamellar BCP films with gold salts led to gold NP arrays with different in plane aspect ratios. Indeed, decorated surfaces consisting of spherical, and rod-like particles with varying degrees of elongation were obtained (Figure 11B). The morphological evolution of the gold NPs has a significant effect on the optical properties of the gold patterns, formed by elongated spheroids, with a high degree of homogeneity, azimuthal isotropy and a gold content as low as 16 vol %producing a refractive index of more than 3 in the visible spectrum (Figure 11B). One of the most important advantages of using BCP self-assembly is the possibility to tune the geometrical parameters of the structure (NP size and interparticle distances) through the macromolecular engineering of the BCP characteristics (molecular weight, composition, and polydispersity). Alvarez–Fernandez and co-workers have recently obtained well-organized arrays of gold nanoparticles of different diameters by the selective impregnation of the hexagonally-ordered cylindrical poly(4-vinylpyridine) domains in self-assembled thin films of PS-*b*-P4VP with different molecular weights (Figure 11C).[243] The morphological and optical properties of the fabricated films were extracted through a modified Bedeaux–Vlieger formalism.[242] This model allows extracting the uniaxial dielectric function for the effective nanoparticle layer, which can be easily integrated into standard thin film analysis software, opening up the possibility of simplifying the metasurface optical characterization.

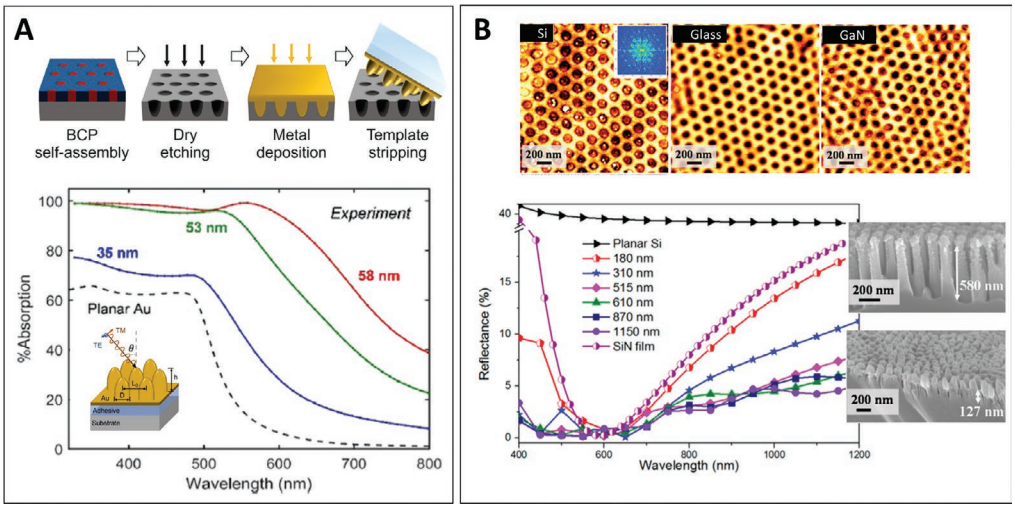

Figure 12. A) Schematic showing the main fabrication steps of the plasmonic metasurfaces (top) and absorption spectra of the nanodome films at normal incidence (bottom). The inset shows a SEM image of the template-stripped gold film with nanodome-like structures. Scale bars 100 nm. Reproduced with permission.[262] Copyright 2018, American Chemical Society. B) AFM topography of the hexagonal BCP films on Si (FFT in the inset), glass and GaN (top). Cross section SEM image of Si and glass nanopillars (right) and simulated reflectance spectra of unpolarized light from nanopillars with different pillar heights compared to planar Si and SiN coated silicon. Reproduced with permission.[264] Copyright 2017, American Chemical Society.

3.5. Absorption and Reflection-Based Metasurfaces

BCP templating has been also applied to produce metal or Si nanostructures to induce absorbing or antireflective surface properties. Such precise control of surfaces and substrates are attractive for sustainable and energy related future technologies, e.g., light harvesters or flexible solar cell panels. This section highlights the diversity of ways to achieve textured surfaces to manipulate light-matter interactions. Hulkkonen and co-workers produced an all metal optical absorber by gold deposition onto etched PS-*b*-P2VP dot patterns followed by a lift-off.[262] **Figure 12**A shows the process flow and SEM images of highly organized gold nanodomes with heights ranging from 44 to 81 nm and base diameters of 30–60 nm. The nanostructured gold film (h = 81 nm) absorbed 97% of incident light from 320 to 650 nm. The process appears highly reproducible and the dry etched Si pores can be used repeatedly to produce the gold nanodome surfaces.

Prior to this work, Bent and co-workers used atomic layer deposition to tune visible light absorption by a gold nanodot coating derived from hexagonal PS-*b*-PMMA BCPs.[263] The authors reported the fabrication of gold nanodots with a 17 nm diameter and a 5 nm height atop an ion-beam deposited SiO_2 layer and an optically thick 90 nm aluminum reflector layer. After depositing a 16 nm SnS_x layer by ALD on the BCP patterned gold nanodots, absorption of ≈93% was achieved in the visible spectrum. Their process highlighted a versatile methodology based an unconventional BCP patterning strategy and industry standard ALD to achieve a highly functional metasurface. Such a process may be useful for large-scale integration in thin film solar cell fabrication. Similarly, Mokarian et al. introduced the use of large BCPs for metal oxide hardmask preparation to produce large period silicon nanopillars (180 ± 18 nm) and diameters (115 ± 19 nm).[264] Importantly, this process showcased the possibility to pattern large linear BCPs to achieve subwavelength Si, glass, and GaN nanostructures. The patterned Si surfaces exhibited very low reflectivities in the VIS/NIR spectrum and maintained similar reflectivities at incident angles as high as 75° (Figure 12B). Moreover, it was shown that the overall scheme could be carried out on curved surfaces. Others have also reported BCP strategies to design broadband antireflective surfaces emphasizing the promise held by such processing for large area fabrication needs.[265–267]

3.6. Other Metallic Plasmonic Metasurfaces

SERS has emerged over the last few decades as a powerful analytical technique that can provide a specific signal fingerprint in complex environments, leading to high sensitivity and multiplexing capabilities.[268] As introduced in Section 2.2, the SERS effect is based on the strong near-field enhancement at the surface of metallic nanoparticles or at junctions between plasmonic nanoparticles in a 2D array. In this sense, BCP based 2D plasmonic metasurfaces have been successfully implemented into SERS biosensors due to their precisely control over size, shape, and spacing of nano-objects at the nanoscale over millimeter-sized areas.[269–271] However, approaches for ultrahigh dense customized periodic metal nanoparticles arrays are still challenging.[272]

Recently, Wang and co-workers have presented a novel route for reliable fabrication of customized periodic metal nanoparticles.[273] Thus, ultradense metal nanogap structures were obtained by evaporation of metallic gold layers over hexagonally packed poly-styrene columns, prepared by thin-film BCP self-assembly (**Figure 13**A). Electric field distribution around the metallic objects created can be conveniently modulated by variation of the nanoscale gap distances via controlled metallic evaporation (Figure 13A). The resultant ultradense plamonic

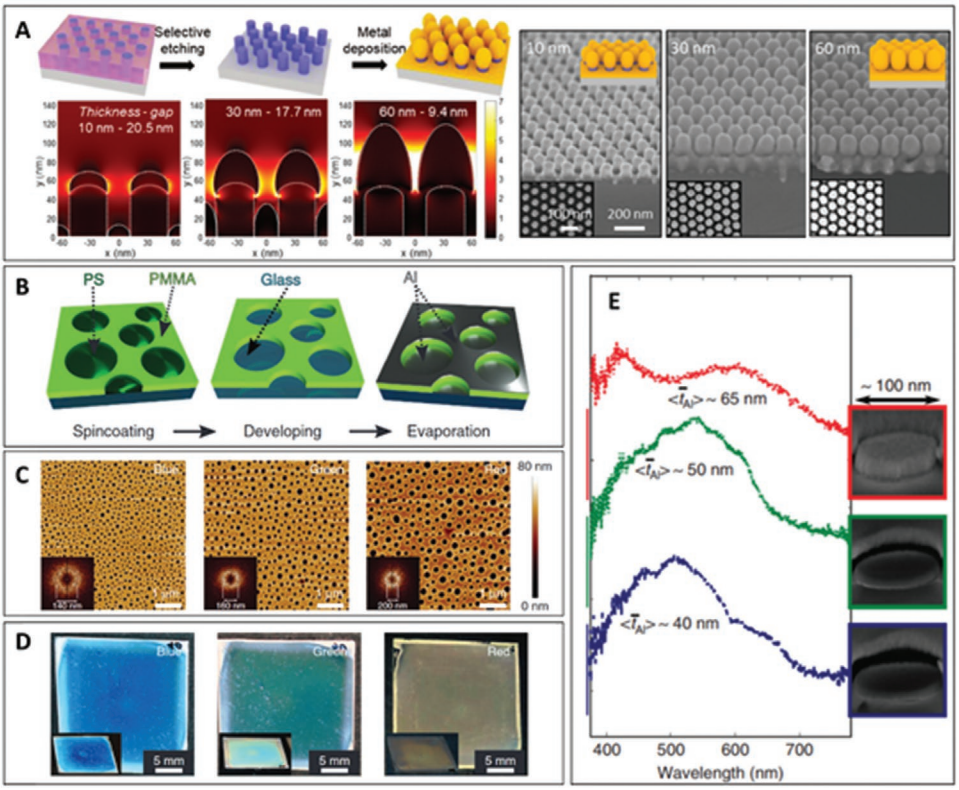

Figure 13. A) Schematic illustration (top) of the formation of ultradense plasmonic metasurfaces array for SERS sensing. SEM images of the nanopatterns created with various metal deposition thicknesses (right) and its effect on the electric-field distribution (bottom). Reproduced with permission.[273] Copyright 2018, American Chemical Society. B) Schematic of the fabrication of aluminum plasmonic metasurfaces by polymer blend lithography. C) AFM images of three samples with different aluminum nanohole-disk pair features diameters. D) Top views of the three samples, showing blue, green, and red colorations. E) Resonance behavior as a function of the Al-layer thickness for a fixed PMMA thickness (70 nm). The spectra indicate a redshift of the dipolar scattering peak with increasing Al thickness. Reproduced with permission.[276] Copyright 2017, Springer Nature.

metasurfaces enables a strong augmentation of Raman intensity, (greater than $\approx 10^4$), allowing a SERS detection limit as low as 100×10^{-9} M.

Although plasmonic research has been mainly focused on gold and silver, other materials, e.g., aluminum or highly doped Si can present comparable plasmonic properties.[274,275] Very recently, Siddique and co-workers have presented a new strategy for the fabrication of plasmonic aluminum metasurfaces based on polymer phase separation.[276] Instead of using a BCP, a blend of two incompatible polymers was used in order to obtain a nanostructured film consisting of randomly oriented circular inclusions of the minor-phase polymer surrounded by the major phase. Chemical etching of one of the polymers followed by the evaporation of a thin aluminum layer on top of the substrate formed the desired structure (Figure 13B). The average dimensions of the scatterers and their density can be easily controlled by the initial blend ratio and thus dictates the optical properties through the tuning of the surface geometrical features (Figure 13C). Indeed, metasurfaces with a high degree of color purity have been obtained by the control of the structural parameters such as aluminum layer thickness or scatterer dimensions (Figure 13D,E). Interestingly, plasmonic aluminum metasurfaces show angle-independent structural colour.[277,278] In view of the above examples, it is evident that today's polymer self-assembly methods represent a very attractive strategy to pattern large-scale plasmonic metasurfaces suitable for visible applications in a timely fashion.

3.7. BCP and Metamaterials, Future Directions

A particular constraint in terms of new functional optical materials based on BCP self-assembly stands out: the intrinsic BCP phase behavior, in particular the minimization of the free energy at the interface between the blocks, limits the variability of structures and symmetries achievable through BCP self-assembly. More complex structures have been proposed of late in order to expand the design space for metaoptics devices.[279,280] Theoretically, the design of more intricate patterns or meta-atoms allows one to manipulate optical beams with higher efficiency. However, these promising new structures face more serious manufacturing challenges than the more conventional designs presented in this review. The different strategies developed in recent years by the BCP community to enrich the variety of structures obtained by BCP self-assembly processes may pave the way to a new generation of on-demand optical metamaterial architectures.

One approach relies on the macromolecular engineering of the BCP chains by the incorporation of additional polymer blocks, forming more complex architectures (from linear to

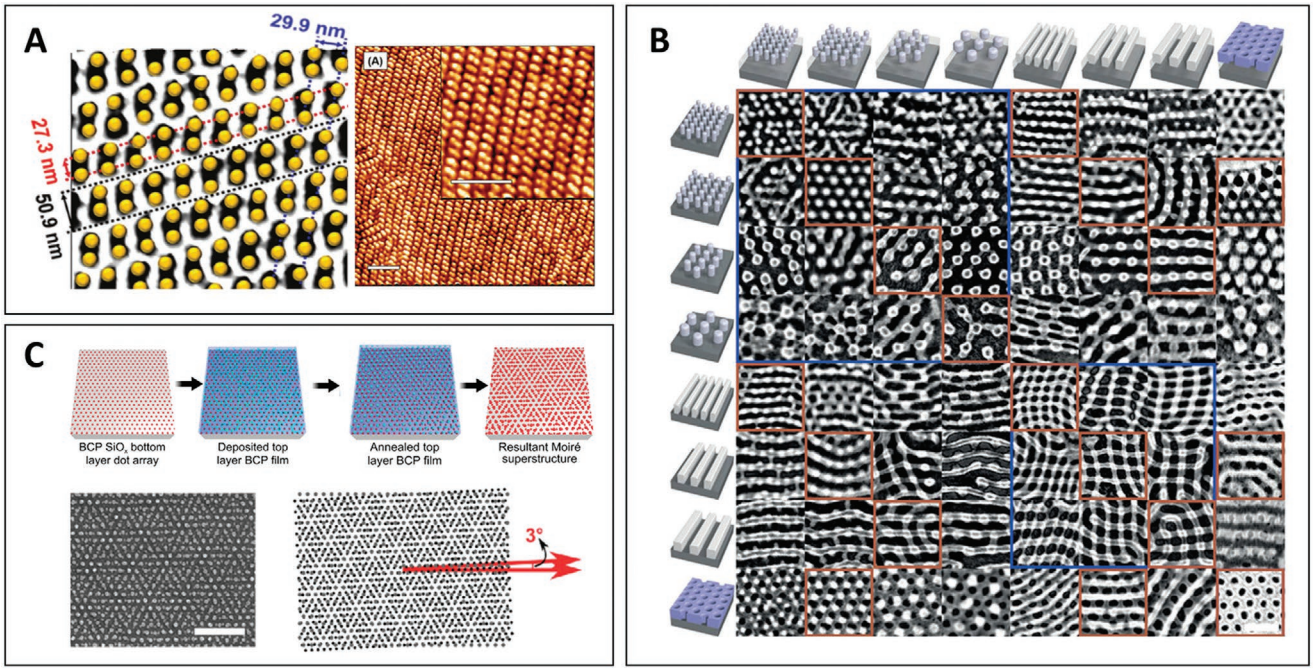

Figure 14. A) Schematic showing the gold dots on the [110] surface of an O^{70} structure, obtained by self-assembly of a linear ABC-type terpolymer (left) and AFM image of the corresponding structure (right). Reproduced with permission.[186] Copyright 2018, Wiley-VCH. B) SEM images showing two-layer nanostructures formed by the iterative self-assembly of the BCP (scale bar: 100 nm). Reproduced with permission.[289] Copyright 2016, Springer Nature. C) Schematic representation (top) and SEM micrographs (bottom) of Moiré superstructures formed from sequential annealing of two incommensurate BCP combinations. Reproduced with permission.[292] Copyright 2017, American Chemical Society.

star, graft, or brush) in order to increase the morphological variety obtained by self-assembly.[281] Aissou and co-workers have recently presented the formation of metallic complex network structures through the self-assembly of linear ABC-type terpolymers.[186] Patterned templates formed by the cubic Q^{214} and orthorhombic O^{70} network structures were used as platforms to build well-ordered gold nanodot thin film arrays with unique 2D $p3m1$ and $p2$ symmetries, respectively. Particularly, the precise control of the gold NP positions within a line/space pattern fabricated from the O^{70} network (see **Figure 14**A), could find very interesting applications as a metasurface design due to the possibility of having a more precise control over the interparticle distances compared with the standard hexagonal packing. Other interesting structures, e.g., hexagonally ordered nanorings,[282–284] square,[285] or hexagonal[286] 2D Archimedean tilings patterns have been recently obtained using a linear terpolymer, supramolecular assembly, and 3-miktoarm star copolymers (Figure 6A).

Another novel concept for the design of complex 3D nanostructures is based on a layering process derived from the iterative self-assembly of BCP layers.[287] Controlled multilayered structures are known as ideal candidates for the design of complex flat optics with a wide variety of functionalities.[288] Pioneering work by Rahman et al.[289] demonstrated the potential application of multilayer BCP self-assembly to produce a large library of 3D structures that are absent in the native BCP phase diagram, including sphere-on-line or line-on-line configurations (see Figure 14B). The possibility to independently control the geometry and function of each layer enables the development of multifunctional devices in which two or more desired optical properties can be independently designed. This sequential layer-by-layer BCP self-assembly technique allows obtaining an unprecedented control over the structural parameters of the different layers.[290] The shape, size and interparticle distances between the different features in each layer can be controlled by choosing a suitable BCP. Interestingly, different metals or nonmetallic species can be selectively introduced into each layer during the fabrication process, giving rise to the possibility of obtaining multicomponent 3D structures. In this sense, Alvarez–Fernandez and co-workers have recently demonstrated the great versatility of this approach, as an alternative and simpler method compared to the colloidal chemistry, in the synthesis of large area multicomponent Al_2O_3–Au raspberry-like nanoclusters.[291] Alternately, Jin and co-workers have shown the application of this strategy for the formation of complex single-grain Moiré superstructures.[292] A first bottom layer of hexagonal silica dots was prepared by self-assembly from a PS-*b*-PDMS block copolymer. A second layer of a PS-*b*-PDMS BCP, with different molecular weight and thus a different periodicity, was then spin-coated onto the initial pattern of silica dots. The registry force of the bottom layer of hexagonally ordered dots is sufficient to direct the self-assembly of the top layer to adopt a preferred relative angle of rotation. Thereby, the combinations of different incommensurate BCPs dots as top and bottom layer leads to different Moiré superstructures (see Figure 14C). This approach constitutes a very promising starting point for the design of new 3D structures, while preserving the low-tech and low-cost nature of the BCP-based processes, and demonstrates the viability of multi-layered BCP self-assembly as straightforward fabrication strategy for complex structure-based optical

metamaterials.[293] In summary, this review has surveyed the vast potential of BCP material demonstrations for dictating optical phenomena derived from metamaterial and metasurface designs. The excellent control we now possess from BCP self-assembly and the unique light matter interactions can lead the way for sophisticated optical device fabrication. One must note that process variability and fab-compatibility (e.g., temperature, nontoxic solvents, humidity effects, and interface effects) in BCP development are a major concern at present, and more robust routes are required, if BCP materials are to be truly considered for future optical metadevices. As outlined above, thin film BCP control and selective infiltration is imperative to produce desired optical behavior and therefore process reproducibility is key. Moreover, this is a multifaceted concern requiring attention to BCP synthesis, film development and postinfiltration of metals/dielectrics. However, in the past 5 years, several encouraging reports have detailed BCP processes that move the field forward and ever closer to meeting fab grade compatibility, e.g., solvent vapor annealing,[294–296] selective material infiltration,[297,298] and defect characterization.[299,300]

4. Conclusions

The field of BCP-based 3D and 2D optical metamaterials has become a promising research direction for next generation optical devices. As illustrated above, BCP templating allows the generation of organized 2D and 3D nanostructures with controlled periodicity and orientation over large areas, offering a straightforward, rapid, and low-cost fabrication strategy for new functional optical materials. Several configurations, e.g., lamellae, cylinders, or gyroids have been used as templates to create optically active architectures, such as metallic and nonmetallic dots, lines, or chiral structures. This review has surveyed the vast potential of BCP-driven material routes for dictating optical phenomena derived from metamaterial and metasurface designs. The excellent control we now possess from BCP self-assembly to foster unique light–matter interactions can lead the way for sophisticated optical device fabrication.

Conflict of Interest

The authors declare no conflict of interest.

Keywords

block copolymers, gyroids, metamaterials, metasurfaces, self-assembly

Received: January 26, 2021
Revised: April 8, 2021
Published online:

[1] J. B. Pendry, A. J. Holden, D. J. Robbins, W. J. Stewart, *IEEE Trans. Microw. Theory Tech.* **1999**, *47*, 2075.
[2] J. Yao, Z. Liu, Y. Liu, Y. Wang, C. Sun, G. Bartal, A. M. Stacy, X. Zhang, *Science* **2008**, *321*, 930.
[3] V. M. Shalaev, W. Cai, U. K. Chettiar, H.-K. Yuan, A. K. Sarychev, V. P. Drachev, A. V. Kildishev, *Opt. Lett.* **2005**, *30*, 3356.
[4] D. R. Smith, W. J. Padilla, D. C. Vier, S. C. Nemat-Nasser, S. Schultz, *Phys. Rev. Lett.* **2000**, *84*, 4184.
[5] A. M. Mahmoud, N. Engheta, *Nat. Commun.* **2014**, *5*, 5638.
[6] K. L. Tsakmakidis, A. D. Boardman, O. Hess, *Nature* **2007**, *450*, 397.
[7] J. B. Pendry, A. J. Holden, W. J. Stewart, I. Youngs, *Phys. Rev. Lett.* **1996**, *76*, 4773.
[8] N. Fang, H. Lee, C. Sun, X. Zhang, *Science* **2005**, *308*, 534.
[9] X. Zhang, Z. Liu, *Nat. Mater.* **2008**, *7*, 435.
[10] J. B. Pendry, *Phys. Rev. Lett.* **2000**, *85*, 3966.
[11] N. Landy, D. R. Smith, *Nat. Mater.* **2013**, *12*, 25.
[12] D. Schurig, J. J. Mock, B. J. Justice, S. A. Cummer, J. B. Pendry, A. F. Starr, D. R. Smith, *Science* **2006**, *314*, 977.
[13] J. Valentine, J. Li, T. Zentgraf, G. Bartal, X. Zhang, *Nat. Mater.* **2009**, *8*, 568.
[14] K. V. Sreekanth, Y. Alapan, M. ElKabbash, E. Ilker, M. Hinczewski, U. A. Gurkan, A. De Luca, G. Strangi, *Nat. Mater.* **2016**, *15*, 621.
[15] X. Xu, B. Peng, D. Li, J. Zhang, L. M. Wong, Q. Zhang, S. Wang, Q. Xiong, *Nano Lett.* **2011**, *11*, 3232.
[16] C. Cao, J. Zhang, X. Wen, S. L. Dodson, N. T. Dao, L. M. Wong, S. Wang, S. Li, A. T. Phan, Q. Xiong, *ACS Nano* **2013**, *7*, 7583.
[17] Y. Dong, T. Itoh, *Proc. IEEE* **2012**, *100*, 2271.
[18] N. I. Landy, S. Sajuyigbe, J. J. Mock, D. R. Smith, W. J. Padilla, *Phys. Rev. Lett.* **2008**, *100*, 207402.
[19] S. B. Glybovski, S. A. Tretyakov, P. A. Belov, Y. S. Kivshar, C. R. Simovski, *Phys. Rep.* **2016**, *634*, 1.
[20] D. R. Smith, J. B. Pendry, M. C. K. Wiltshire, *Science* **2004**, *305*, 788.
[21] Y. Liu, X. Zhang, *Chem. Soc. Rev.* **2011**, *40*, 2494.
[22] C. M. Soukoulis, M. Wegener, *Nat. Photonics* **2011**, *5*, 523.
[23] Y. Xie, C. Yang, Y. Wang, Y. Shen, X. Deng, B. Zhou, J. Cao, *Sci. Rep.* **2019**, *9*, 1.
[24] M. Decker, N. Feth, C. M. Soukoulis, S. Linden, M. Wegener, *Phys. Rev. B* **2011**, *84*, 085416.
[25] M. C. Gwinner, E. Koroknay, L. Fu, P. Patoka, W. Kandulski, M. Giersig, H. Giessen, *Small* **2009**, *5*, 400.
[26] J. Valentine, S. Zhang, T. Zentgraf, E. Ulin-Avila, D. A. Genov, G. Bartal, X. Zhang, *Nature* **2008**, *455*, 376.
[27] N. Liu, H. Guo, L. Fu, S. Kaiser, H. Schweizer, H. Giessen, *Nat. Mater.* **2008**, *7*, 31.
[28] W. Wu, E. Kim, E. Ponizovskaya, Y. Liu, Z. Yu, N. Fang, Y. R. Shen, A. M. Bratkovsky, W. Tong, C. Sun, X. Zhang, S. Y. Wang, R. S. Williams, *Appl. Phys. A: Mater. Sci. Process.* **2007**, *87*, 143.
[29] T. Ergin, N. Stenger, P. Brenner, J. B. Pendry, M. Wegener, *Science* **2010**, *328*, 337.
[30] Q. Yang, J. Gu, D. Wang, X. Zhang, Z. Tian, C. Ouyang, R. Singh, J. Han, W. Zhang, *Opt. Express* **2014**, *22*, 25931.
[31] S. Zhang, M.-H. Kim, F. Aieta, A. She, T. Mansuripur, I. Gabay, M. Khorasaninejad, D. Rousso, X. Wang, M. Troccoli, N. Yu, F. Capasso, *Opt. Express* **2016**, *24*, 18024.
[32] B. Ratni, A. de Lustrac, G. P. Piau, S. N. Burokur, *Appl. Phys. A: Mater. Sci. Process.* **2018**, *124*, 104.
[33] B. Ratni, A. de Lustrac, G.-P. Piau, S. N. Burokur, *Opt. Express* **2018**, *26*, 2613.
[34] Y. Yuan, K. Zhang, X. Ding, B. Ratni, S. N. Burokur, Q. Wu, *Photonics Res.* **2019**, *7*, 80.
[35] J. K. Gansel, M. Thiel, M. S. Rill, M. Decker, K. Bade, V. Saile, G. Von Freymann, S. Linden, M. Wegener, *Science* **2009**, *325*, 1513.
[36] A. Radke, T. Gissibl, T. Klotzbücher, P. V. Braun, H. Giessen, *Adv. Mater.* **2011**, *23*, 3018.
[37] R. Liu, C. Ji, Z. Zhao, T. Zhou, *Engineering* **2015**, *1*, 179.
[38] S. Ji, L. Wan, C. C. Liu, P. F. Nealey, *Prog. Polym. Sci.* **2016**, *54–55*, 76.

[39] W. Li, M. Müller, *Prog. Polym. Sci.* **2016**, *54–55*, 47.
[40] Y. H. Ye, S. Badilescu, V. Van Truong, P. Rochon, A. Natansohn, *Appl. Phys. Lett.* **2001**, *79*, 872.
[41] J. F. Galisteo-Lõpez, M. Ibisate, R. Sapienza, L. S. Froufe-Pérez, Ú. Blanco, C. Lõpez, *Adv. Mater.* **2011**, *23*, 30.
[42] S. H. Kim, J. M. Lim, S. K. Lee, C. J. Heo, S. M. Yang, *Soft Matter.* **2010**, *6*, 1092.
[43] S. H. Kim, S. Y. Lee, S. M. Yang, G. R. Yi, *NPG Asia Mater.* **2011**, *3*, 25.
[44] N. Vogel, M. Retsch, C. A. Fustin, A. Del Campo, U. Jonas, *Chem. Rev.* **2015**, *115*, 6265.
[45] P. A. Kralchevsky, K. Nagayama, *Langmuir* **1994**, *10*, 23.
[46] J. Angly, A. Iazzolino, J. B. Salmon, J. Leng, S. P. Chandran, V. Ponsinet, A. Désert, A. Le Beulze, S. Mornet, M. Tréguer-Delapierre, M. A. Correa-Duarte, *ACS Nano* **2013**, *7*, 6465.
[47] L. Mishchenko, B. Hatton, M. Kolle, J. Aizenberg, *Small* **2012**, *8*, 1904.
[48] C. E. Finlayson, J. J. Baumberg, *Polym. Int.* **2013**, *62*, 1403.
[49] S. Wong, V. Kitaev, G. A. Ozin, *J. Am. Chem. Soc.* **2003**, *125*, 15589.
[50] K. Bian, H. Schunk, D. Ye, A. Hwang, T. S. Luk, R. Li, Z. Wang, H. Fan, *Nat. Commun.* **2018**, *9*, 2365.
[51] N. Vogel, S. Utech, G. T. England, T. Shirman, K. R. Phillips, N. Koay, I. B. Burgess, M. Kolle, D. A. Weitz, J. Aizenberg, *Proc. Natl. Acad. Sci. USA* **2015**, *112*, 10845.
[52] T. B. Hoang, G. M. Akselrod, C. Argyropoulos, J. Huang, D. R. Smith, M. H. Mikkelsen, *Nat. Commun.* **2015**, *6*, 7788.
[53] Y. Brasse, M. B. Müller, M. Karg, C. Kuttner, T. A. F. König, A. Fery, *ACS Appl. Mater. Interfaces* **2018**, *10*, 3133.
[54] M. B. Müller, C. Kuttner, T. A. F. König, V. V. Tsukruk, S. Förster, M. Karg, A. Fery, *ACS Nano* **2014**, *8*, 9410.
[55] K. Volk, J. P. S. Fitzgerald, M. Retsch, M. Karg, *Adv. Mater.* **2015**, *27*, 7332.
[56] T. A. F. König, P. A. Ledin, J. Kerszulis, M. A. Mahmoud, M. A. El-Sayed, J. R. Reynolds, V. V. Tsukruk, *ACS Nano* **2014**, *8*, 6182.
[57] R. G. Freeman, K. C. Grabar, K. J. Allison, R. M. Bright, J. A. Davis, A. P. Guthrie, M. B. Hommer, M. A. Jackson, P. C. Smith, D. G. Walter, M. J. Natan, *Science* **1995**, *267*, 1629.
[58] S. R. Smith, J. Lipkowski, *J. Phys. Chem. C* **2018**, *122*, 7303.
[59] A. X. Wang, X. Kong, *Materials* **2015**, *8*, 3024.
[60] F. Romano, F. Sciortino, *Nat. Publ. Gr.* **2011**, *10*, 171.
[61] W. B. Rogers, W. M. Shih, V. N. Manoharan, *Nat. Rev. Mater.* **2016**, *1*, 16008.
[62] R. Schreiber, N. Luong, Z. Fan, A. Kuzyk, P. C. Nickels, T. Zhang, D. M. Smith, B. Yurke, W. Kuang, A. O. Govorov, T. Liedl, *Nat. Commun.* **2013**, *4*, 2948.
[63] V. Liljeström, A. Ora, J. Hassinen, H. T. Rekola, N. Nonappa, M. Heilala, V. Hynninen, J. J. Joensuu, R. H. A. Ras, P. Törmä, O. Ikkala, M. A. Kostiainen, *Nat. Commun.* **2017**, *8*, 671.
[64] M. A. Boles, M. Engel, D. V. Talapin, *Chem. Rev.* **2016**, *116*, 11220.
[65] M. Stefik, S. Guldin, S. Vignolini, U. Wiesner, U. Steiner, *Chem. Soc. Rev.* **2015**, *44*, 5076.
[66] A. B. Chang, F. S. Bates, *Macromolecules* **2020**, *53*, 2765.
[67] H. C. Kim, S. M. Park, W. D. Hinsberg, I. R. Division, *Chem. Rev.* **2010**, *110*, 146.
[68] A. Alvarez-Fernandez, K. Aissou, G. Pécastaings, G. Hadziioannou, G. Fleury, V. Ponsinet, *Nanoscale Adv.* **2019**, *1*, 849.
[69] S. Salvatore, A. Demetriadou, S. Vignolini, S. S. Oh, S. Wuestner, N. A. Yufa, M. Stefik, U. Wiesner, J. J. Baumberg, O. Hess, U. Steiner, *Adv. Mater.* **2013**, *25*, 2713.
[70] S. Vignolini, N. A. Yufa, P. S. Cunha, S. Guldin, I. Rushkin, M. Stefik, K. Hur, U. Wiesner, J. J. Baumberg, U. Steiner, *Adv. Mater.* **2012**, *24*, OP23.
[71] X. Wang, K. Ehrhardt, C. Tallet, M. Warenghem, A. Baron, A. Aradian, M. Kildemo, V. Ponsinet, *Opt. Laser Technol.* **2017**, *88*, 85.
[72] J. Y. Kim, H. Kim, B. H. Kim, T. Chang, J. Lim, H. M. Jin, J. H. Mun, Y. J. Choi, K. Chung, J. Shin, S. Fan, S. O. Kim, *Nat. Commun.* **2016**, *7*, 12911.
[73] S. Liu, Y. Yang, L. Zhang, J. Xu, J. Zhu, *J. Mater. Chem. C* **2020**, *8*, 16633.
[74] K. Wang, S. H. Park, J. Zhu, J. K. Kim, L. Zhang, G. R. Yi, *Adv. Funct. Mater.* **2020**, *31*, 2008246.
[75] J. Mistrik, S. Kasap, H. E. Ruda, C. Koughia, J. Singh, *Springer Handbooks*, Springer, Berlin **2017**, p. 1.
[76] J. B. Pendry, A. J. Holden, D. J. Robbins, W. J. Stewart, *IEEE Trans. Microwave Theory Tech.* **1999**, *47*, 2075.
[77] T. J. Yen, *Science* **2004**, *303*, 1494.
[78] L. D. Landau, E. M. Lifshitz, L. P. Pitaevskii, *Electrodynamics of Continuous Media*, Course of Theoretical Physics, Vol. *8*, Butterworth-Heinemann, Oxford **1984**.
[79] C. Kilchoer, N. Abdollahi, J. A. Dolan, D. Abdelrahman, M. Saba, U. Wiesner, U. Steiner, I. Gunkel, B. D. Wilts, *Adv. Opt. Mater.* **2020**, *8*, 1902131.
[80] J. M. Hamm, S. Wuestner, K. L. Tsakmakidis, O. Hess, *Phys. Rev. Lett.* **2011**, *107*, 167405.
[81] S. S. Kruk, D. A. Powell, A. Minovich, D. N. Neshev, Y. S. Kivshar, *Opt. Express* **2012**, *20*, 15100.
[82] M. G. Silveirinha, C. A. Fernandes, *IEEE Trans. Microwave Theory Tech.* **2005**, *53*, 1418.
[83] A. Demetriadou, J. B. Pendry, *J. Phys.: Condens. Matter* **2008**, *20*, 295222.
[84] A. Baron, A. Aradian, V. Ponsinet, P. Barois, *Comptes Rendus Phys.* **2020**, *21*, 443.
[85] I. Staude, A. E. Miroshnichenko, M. Decker, N. T. Fofang, S. Liu, E. Gonzales, J. Dominguez, T. S. Luk, D. N. Neshev, I. Brener, Y. Kivshar, *ACS Nano* **2013**, *7*, 7824.
[86] A. B. Evlyukhin, S. M. Novikov, U. Zywietz, R. L. Eriksen, C. Reinhardt, S. I. Bozhevolnyi, B. N. Chichkov, *Nano Lett.* **2012**, *12*, 3749.
[87] Q. Zhao, L. Kang, B. Du, H. Zhao, Q. Xie, X. Huang, B. Li, J. Zhou, L. Li, *Phys. Rev. Lett.* **2008**, *101*, 027402.
[88] C. L. Holloway, E. F. Kuester, J. Baker-Jarvis, P. Kabos, *IEEE Trans. Antennas Propag.* **2003**, *51*, 2596.
[89] S. A. Maier, *Plasmonics: Fundamentals and Applications*, Springer, New York, **2007**.
[90] D. Sevenler, N. Lortlar Ünlü, M. S. Ünlü, *Nanobiosensors and Nanobioanalyses*, Springer, Japan, **2015**, pp. 81–95.
[91] A. Schönhardt, D. Nau, C. Bauer, A. Christ, H. Gräbeldinger, H. Giessen, *Philos. Trans. R. Soc., A* **2017**, *375*, 20160065.
[92] T. Chung, S.-Y. Lee, E. Y. Song, H. Chun, B. Lee, *Sensors* **2011**, *11*, 10907.
[93] M. Moskovits, *J. Raman Spectrosc.* **2005**, *36*, 485.
[94] A. M. Funston, C. Novo, T. J. Davis, P. Mulvaney, *Nano Lett.* **2009**, *9*, 1651.
[95] S. Lamowski, C. R. Mann, F. Hellbach, E. Mariani, G. Weick, F. Pauly, *Phys. Rev. B* **2018**, *97*, 125409.
[96] A. V. Chebykin, M. A. Gorlach, P. A. Belov, *Phys. Rev. B: Condens. Matter Mater. Phys.* **2015**, *92*, 045127.
[97] M. Saba, J. M. Hamm, J. J. Baumberg, O. Hess, *Phys. Rev. Lett.* **2017**, *119*, 227401.
[98] V. G. Kravets, F. Schedin, A. N. Grigorenko, *Phys. Rev. Lett.* **2008**, *101*, 087403.
[99] W. Wang, M. Ramezani, A. I. Väkeväinen, P. Törmä, J. G. Rivas, T. W. Odom, *Mater. Today* **2018**, *21*, 303.
[100] V. G. Kravets, A. V. Kabashin, W. L. Barnes, A. N. Grigorenko, *Chem. Rev.* **2018**, *118*, 5912.
[101] C. Li, M. Iqbal, J. Lin, X. Luo, B. Jiang, V. Malgras, K. C. W. Wu, J. Kim, Y. Yamauchi, *Acc. Chem. Res.* **2018**, *51*, 1764.

[102] S. Salvatore, A. Demetriadou, S. Vignolini, S. S. Oh, S. Wuestner, N. A. Yufa, M. Stefik, U. Wiesner, J. J. Baumberg, O. Hess, U. Steiner, *Adv. Mater.* **2013**, *25*, 2713.
[103] A. Demetriadou, J. B. Pendry, *J. Phys. Condens. Matter* **2009**, *21*, 376003.
[104] Z. Wang, F. Cheng, T. Winsor, Y. Liu, *Nanotechnology* **2016**, *27*, 412001.
[105] W. J. Chen, B. Hou, Z. Q. Zhang, J. B. Pendry, C. T. Chan, *Nat. Commun.* **2018**, *9*, 1.
[106] K. Hur, Y. Francescato, V. Giannini, S. A. Maier, R. G. Hennig, U. Wiesner, *Angew. Chem., Int. Ed.* **2011**, *50*, 11985.
[107] J. A. Dolan, R. Dehmel, A. Demetriadou, Y. Gu, U. Wiesner, T. D. Wilkinson, I. Gunkel, O. Hess, J. J. Baumberg, U. Steiner, M. Saba, B. D. Wilts, *Adv. Mater.* **2019**, *31*, 1803478.
[108] W. Zhou, T. W. Odom, *Nat. Nanotechnol.* **2011**, *6*, 423.
[109] R. A. Shelby, D. R. Smith, S. Schultz, *Science* **2001**, *292*, 77.
[110] V. G. Veselago, *Fiz. Nauk* **1968**, *92*, 517.
[111] J. B. Pendry, D. Schurig, D. R. Smith, *Science* **2006**, *312*, 1780.
[112] N. Liu, H. Guo, L. Fu, S. Kaiser, H. Schweizer, H. Giessen, *Nat. Mater.* **2008**, *7*, 31.
[113] S. Mühlig, C. Rockstuhl, V. Yannopapas, T. Bürgi, N. Shalkevich, F. Lederer, *Opt. Express* **2011**, *19*, 9607.
[114] L. Malassis, P. Massé, M. Tréguer-Delapierre, S. Mornet, P. Weisbecker, V. Kravets, A. Grigorenko, P. Barois, *Langmuir* **2013**, *29*, 1551.
[115] S. Gomez-Graña, A. Le Beulze, M. Treguer-Delapierre, S. Mornet, E. Duguet, E. Grana, E. Cloutet, G. Hadziioannou, J. Leng, J.-B. Salmon, V. G. Kravets, A. N. Grigorenko, N. A. Peyyety, V. Ponsinet, P. Richetti, A. Baron, D. Torrent, P. Barois, *Mater. Horiz.* **2016**, *3*, 596.
[116] X. Zhang, Y. Wu, *Sci. Rep.* **2015**, *5*, 1.
[117] J. B. Pendry, *Science* **2004**, *306*, 1353.
[118] N. Guth, B. Gallas, J. Rivory, J. Grand, A. Ourir, G. Guida, R. Abdeddaim, C. Jouvaud, J. De Rosny, *Phys. Rev. B: Condens. Matter Mater. Phys.* **2012**, *85*, 115138.
[119] S. Zhang, W. Fan, N. C. Panoiu, K. J. Malloy, R. M. Osgood, S. R. J. Brueck, *Phys. Rev. Lett.* **2005**, *95*, 137404.
[120] S. S. Bukhari, J. Vardaxoglou, W. Whittow, *Appl. Sci.* **2019**, *9*, 2727.
[121] H. T. Chen, A. J. Taylor, N. Yu, *Rep. Prog. Phys.* **2016**, *79*, 076401.
[122] F. Ding, A. Pors, S. I. Bozhevolnyi, *Rep. Prog. Phys.* **2018**, *81*, 026401.
[123] S. Chang, X. Guo, X. Ni, *Annu. Rev. Mater. Res.* **2018**, *48*, 279.
[124] R. Dezert, P. Richetti, A. Baron, *Opt. Express* **2019**, *27*, 26317.
[125] W. T. Chen, A. Y. Zhu, F. Capasso, *Nat. Rev. Mater.* **2020**, *5*, 604.
[126] B. Orazbayev, N. Mohammadi Estakhri, A. Alù, M. Beruete, *Adv. Opt. Mater.* **2017**, *5*, 1600606.
[127] H. Wakatsuchi, S. Kim, J. J. Rushton, D. F. Sievenpiper, *Phys. Rev. Lett.* **2013**, *111*, 245501.
[128] G. V. Eleftheriades, *Nature* **2014**, *505*, 490.
[129] Z. Li, X. Cai, L. Huang, H. Xu, Y. Wei, N. Dai, *Adv. Theory Simul.* **2019**, *2*, 1900086.
[130] C. Pfeiffer, A. Grbic, *Phys. Rev. Lett.* **2013**, *110*, 197401.
[131] K. Chen, Y. Feng, F. Monticone, J. Zhao, B. Zhu, T. Jiang, L. Zhang, Y. Kim, X. Ding, S. Zhang, A. Alù, C. W. Qiu, *Adv. Mater.* **2017**, *29*, 1606422.
[132] M. Decker, I. Staude, M. Falkner, J. Dominguez, D. N. Neshev, I. Brener, T. Pertsch, Y. S. Kivshar, *Adv. Opt. Mater.* **2015**, *3*, 813.
[133] B. H. Fong, J. S. Colburn, J. J. Ottusch, J. L. Visher, D. F. Sievenpiper, *IEEE Trans. Antennas Propag.* **2010**, *58*, 3212.
[134] C. Caloz, *Mater. Today* **2009**, *12*, 12.
[135] A. V. Goncharenko, E. F. Venger, A. O. Pinchuk, *Opt. Express* **2014**, *22*, 2429.
[136] J. P. Lombardi, R. A. Coutu, *Conf. Proc. Soc. Exp. Mech. Ser.*, Springer, New York **2011**, pp. 151–158.
[137] W. H. Weber, G. W. Ford, *Phys. Rev. B: Condens. Matter Mater. Phys.* **2004**, *70*, 125429.
[138] G. Aguirregabiria, J. Aizpurua, R. Esteban, *Opt. Express* **2017**, *25*, 13760.
[139] A. Alù, N. Engheta, *Phys. Rev. B: Condens. Matter Mater. Phys.* **2006**, *74*, 205436.
[140] W. P. Su, J. R. Schrieffer, A. J. Heeger, *Phys. Rev. Lett.* **1979**, *42*, 1698.
[141] S. R. Pocock, X. Xiao, P. A. Huidobro, V. Giannini, *ACS Photonics* **2018**, *5*, 2271.
[142] H. T. Rekola, T. K. Hakala, P. Törmä, *ACS Photonics* **2018**, *5*, 1822.
[143] F. S. Bates, G. H. Fredrickson, *Phys. Today* **1999**, *52*, 32.
[144] M. Fixman, *J. Chem. Phys.* **1962**, *36*, 306.
[145] F. S. Bates, G. H. Fredrickson, *Annu. Rev. Phys. Chem.* **1990**, *41*, 525.
[146] L. Leibler, *Macromolecules* **1980**, *13*, 1602.
[147] A. K. Khandpur, S. Förster, F. S. Bates, I. W. Hamley, A. J. Ryan, W. Bras, K. Almdal, K. Mortensen, *Macromolecules* **1995**, *28*, 8796.
[148] S. Förster, A. K. Khandpur, J. Zhao, F. S. Bates, I. W. Hamley, A. J. Ryan, W. Bras, *Macromolecules* **1994**, *27*, 6922.
[149] F. S. Bates, M. F. Schulz, A. K. Khandpur, S. Förster, J. H. Rosedale, K. Almdal, K. Mortensen, *Faraday Discuss.* **1994**, *98*, 7.
[150] I. Botiz, S. B. Darling, *Mater. Today* **2010**, *13*, 42.
[151] C. Sinturel, M. Vayer, M. Morris, M. A. Hillmyer, *Macromolecules* **2013**, *46*, 5399.
[152] A. Knoll, A. Horvat, K. S. Lyakhova, G. Krausch, G. J. A. Sevink, A. V. Zvelindovsky, R. Magerle, *Phys. Rev. Lett.* **2002**, *89*, 035501.
[153] R. A. Segalman, *Mater. Sci. Eng., R* **2005**, *48*, 191.
[154] T. H. Epps, D. M. DeLongchamp, M. J. Fasolka, D. A. Fischer, E. L. Jablonski, *Langmuir* **2007**, *23*, 3355.
[155] E. Han, K. O. Stuen, M. Leolukman, C.-C. Liu, P. F. Nealey, P. Gopalan, *Macromolecules* **2009**, *42*, 4896.
[156] P. Mansky, Y. Liu, E. Huang, T. P. Russell, C. Hawker, *Science* **1997**, *275*, 1458.
[157] C. M. Bates, T. Seshimo, M. J. Maher, W. J. Durand, J. D. Cushen, L. M. Dean, G. Blachut, C. J. Ellison, C. G. Willson, *Science* **2012**, *338*, 775.
[158] B. Sarkar, P. Alexandridis, *Prog. Polym. Sci.* **2015**, *40*, 33.
[159] T. N. Hoheisel, K. Hur, U. B. Wiesner, *Prog. Polym. Sci.* **2015**, *40*, 3.
[160] C. Cummins, M. A. Morris, *Microelectron. Eng.* **2018**, *195*, 74.
[161] S. S. Lamarre, A. Sarrazin, J. Proust, H. Yockell-Lelièvre, J. Plain, A. M. Ritcey, T. Maurer, *J. Nanopart. Res.* **2013**, *15*, 1656.
[162] S. S. Lamarre, C. Lemay, C. Labrecque, A. M. Ritcey, *Langmuir* **2013**, *29*, 10891.
[163] Q. Li, J. He, E. Glogowski, X. Li, J. Wang, T. Emrick, T. P. Russell, *Adv. Mater.* **2008**, *20*, 1462.
[164] F. Aubrit, F. Testard, A. Paquirissamy, F. Gobeaux, X. Wang, F. Nallet, P. Fontaine, V. Ponsinet, P. Guenoun, *J. Mater. Chem. C* **2018**, *6*, 8194.
[165] S. C. Warren, L. C. Messina, L. S. Slaughter, M. Kamperman, Q. Zhou, S. M. Gruner, F. J. DiSalvo, U. Wiesner, *Science* **2008**, *320*, 1748.
[166] K. Aissou, T. Alnasser, G. Pecastaings, G. Goglio, O. Toulemonde, S. Mornet, G. Fleury, G. Hadziioannou, *J. Mater. Chem. C* **2013**, *1*, 1317.
[167] B. Reid, A. Taylor, A. Alvarez-Fernandez, M. H. Ismael, S. Sharma, B. Schmidt-Hansberg, S. Guldin, *ACS Appl. Mater. Interfaces* **2019**, *11*, 19308.
[168] A. J. Hong, C.-C. Liu, Y. Wang, J. Kim, F. Xiu, S. Ji, J. Zou, P. F. Nealey, K. L. Wang, *Nano Lett.* **2010**, *10*, 224.
[169] H.-S. Moon, J. Y. Kim, H. M. Jin, W. J. Lee, H. J. Choi, J. H. Mun, Y. J. Choi, S. K. Cha, S. H. Kwon, S. O. Kim, *Adv. Funct. Mater.* **2014**, *24*, 4343.
[170] J. W. Elam, M. Biswas, S. B. Darling, A. Yanguas-Gil, J. D. Emery, A. B. F. Martinson, P. F. Nealey, T. Segal-Peretz, Q. Peng, J. Winterstein, J. A. Liddle, Y.-C. Tseng, *ECS Trans.* **2015**, *69*, 147.

[171] B. Gong, Q. Peng, J. S. Jur, C. K. Devine, K. Lee, G. N. Parsons, *Chem. Mater.* **2011**, *23*, 3476.
[172] A. Subramanian, N. Tiwale, C. Y. Nam, *JOM* **2019**, *71*, 185.
[173] I. Weisbord, N. Shomrat, R. Azoulay, A. Kaushansky, T. Segal-Peretz, *Chem. Mater.* **2020**, *32*, 4499.
[174] J. Yin, Q. Xu, Z. Wang, X. Yao, Y. Wang, *J. Mater. Chem. C* **2013**, *1*, 1029.
[175] Q. Peng, Y. C. Tseng, Y. Long, A. U. Mane, S. DiDona, S. B. Darling, J. W. Elam, *Langmuir* **2017**, *33*, 13214.
[176] P. Mokarian-Tabari, R. Senthamaraikannan, C. Glynn, T. W. Collins, C. Cummins, D. Nugent, C. O'Dwyer, M. A. Morris, *Nano Lett.* **2017**, *17*, 2973.
[177] J.-J. Zou, Y. Zhang, C.-J. Liu, *Langmuir* **2006**, *22*, 11388.
[178] A. Alexandrov, L. Smirnova, N. Yakimovich, N. Sapogova, L. Soustov, A. Kirsanov, N. Bityurin, *Appl. Surf. Sci.* **2005**, *248*, 181.
[179] D. O. Shin, J. H. Mun, G.-T. Hwang, J. M. Yoon, J. Y. Kim, J. M. Yun, Y.-B. Yang, Y. Oh, J. Y. Lee, J. Shin, K. J. Lee, S. Park, J. U. Kim, S. O. Kim, *ACS Nano* **2013**, *7*, 8899.
[180] J. Chai, D. Wang, X. Fan, J. M. Buriak, *Nat. Nanotechnol.* **2007**, *2*, 500.
[181] T. Ghoshal, M. T. Shaw, C. T. Bolger, J. D. Holmes, M. A. Morris, *J. Mater. Chem.* **2012**, *22*, 12083.
[182] C. Cummins, T. Ghoshal, J. D. Holmes, M. A. Morris, *Adv. Mater.* **2016**, *28*, 5586.
[183] K. Shin, K. A. Leach, J. T. Goldbach, D. H. Kim, J. Y. Jho, M. Tuominen, C. J. Hawker, T. P. Russell, *Nano Lett.* **2002**, *2*, 933.
[184] D. Borah, M. T. Shaw, S. Rasappa, R. A. Farrell, C. O'Mahony, C. M. Faulkner, M. Bosea, P. Gleeson, J. D. Holmes, M. A. Morris, *J. Phys. D: Appl. Phys.* **2011**, *44*, 174012.
[185] X. Li, J. Iocozzia, Y. Chen, S. Zhao, X. Cui, W. Wang, H. Yu, S. Lin, Z. Lin, *Angew. Chem., Int. Ed.* **2018**, *57*, 2046.
[186] K. Aissou, M. Mumtaz, A. Alvarez-Fernandez, J. Mercat, S. Antoine, G. Pécastaings, V. Ponsinet, C. Dobrzynski, G. Fleury, G. Hadziioannou, *Macromol. Rapid Commun.* **2018**, *39*, 1700754.
[187] J. Chai, J. M. Buriak, *ACS Nano* **2008**, *2*, 489.
[188] T. Ghoshal, T. Maity, J. F. Godsell, S. Roy, M. A. Morris, *Adv. Mater.* **2012**, *24*, 2390.
[189] M. K. Mayeda, J. Hayat, T. H. Epps, J. Lauterbach, *J. Mater. Chem. A* **2015**, *3*, 7822.
[190] C. Cummins, A. Gangnaik, R. A. Kelly, D. Borah, J. O'Connell, N. Petkov, Y. M. Georgiev, J. D. Holmes, M. A. Morris, *Nanoscale* **2015**, *7*, 6712.
[191] S. Xiao, X. Yang, E. W. Edwards, Y.-H. La, P. F. Nealey, *Nanotechnology* **2005**, *16*, S324.
[192] D. Zschech, D. H. Kim, A. P. Milenin, S. Hopfe, R. Scholz, P. Göring, R. Hillebrand, S. Senz, C. J. Hawker, T. P. Russell, M. Steinhart, U. Gösele, *Nanotechnology* **2006**, *17*, 2122.
[193] S. Park, B. Kim, A. Cirpan, T. P. Russell, *Small* **2009**, *5*, 1343.
[194] S. Salvatore, S. Vignolini, J. Philpott, M. Stefik, U. Wiesner, J. J. Baumberg, U. Steiner, *Nanoscale* **2015**, *7*, 1032.
[195] S. N. Abdollahi, E. Ochoa Martínez, C. Kilchoer, G. Kremer, T. Jaouen, P. Aebi, T. Hellmann, T. Mayer, Y. Gu, U. B. Wiesner, U. Steiner, B. D. Wilts, I. Gunkel, *Adv. Mater. Interfaces* **2020**, *7*, 2001227.
[196] S. S. Oh, A. Demetriadou, S. Wuestner, O. Hess, *Adv. Mater.* **2013**, *25*, 612.
[197] B. Wood, J. B. Pendry, D. P. Tsai, *Phys. Rev. B* **2006**, *74*, 115116.
[198] A. Demetriadou, S. S. Oh, S. Wuestner, O. Hess, *New J. Phys.* **2012**, *14*, 083032.
[199] (Ed.: M. I. Aroyo), *International Tables for Crystallography, Volume A: Space-Group Symmetry*, Springer, New York 1983.
[200] S. T. Hyde, M. O'Keeffe, D. M. Proserpio, *Angew. Chem., Int. Ed.* **2008**, *47*, 7996.
[201] O. Delgado Friedrichs, M. O'Keeffe, O. M. Yaghi, *Acta Crystallogr., Sect. A: Found. Crystallogr.* **2003**, *59*, 22.
[202] K. Große-Brauckmann, *Exp. Math.* **1997**, *6*, 33.
[203] M. Saba, B. D. Wilts, J. Hielscher, G. E. Schröder-Turk, *Mater. Today: Proc.* **2014**, *1S*, 193.
[204] J. A. Dolan, B. D. Wilts, S. Vignolini, J. J. Baumberg, U. Steiner, T. D. Wilkinson, *Adv. Opt. Mater.* **2015**, *3*, 12.
[205] B. P. Cumming, G. E. Schröder-Turk, M. Gu, *Opt. Lett.* **2018**, *43*, 863.
[206] M. D. Turner, M. Saba, Q. Zhang, B. P. Cumming, G. E. Schröder-Turk, M. Gu, *Nat. Photonics* **2013**, *7*, 801.
[207] M. Saba, M. Thiel, M. D. Turner, S. T. Hyde, M. Gu, K. Grosse-Brauckmann, D. N. Neshev, K. Mecke, G. E. Schröder-Turk, *Phys. Rev. Lett.* **2011**, *106*, 103902.
[208] M. Saba, M. D. Turner, K. Mecke, M. Gu, G. E. Schröder-Turk, *Phys. Rev. B: Condens. Matter Mater. Phys.* **2013**, *88*, 245116.
[209] B. P. Cumming, G. E. Schröder-Turk, S. Debbarma, M. Gu, *Light Sci. Appl.* **2017**, *6*, e16192.
[210] F. Turella, B. P. Cumming, G. E. Schröder-Turk, M. Gu, *Opt. Lett.* **2015**, *40*, 4795.
[211] P. Farah, A. Demetriadou, S. Salvatore, S. Vignolini, M. Stefik, U. Wiesner, O. Hess, U. Steiner, V. K. Valev, J. J. Baumberg, *Phys. Rev. Appl.* **2014**, *2*, 044002.
[212] J. A. Dolan, R. Dehmel, A. Demetriadou, Y. Gu, U. Wiesner, T. D. Wilkinson, I. Gunkel, O. Hess, J. J. Baumberg, U. Steiner, M. Saba, B. D. Wilts, *Adv. Mater.* **2019**, *31*, 1803478.
[213] C. Kilchoer, N. Abdollahi, J. A. Dolan, D. Abdelrahman, M. Saba, U. Wiesner, U. Steiner, I. Gunkel, B. D. Wilts, *Adv. Opt. Mater.* **2020**, *8*, 1902131.
[214] K. Hur, Y. Francescato, V. Giannini, S. A. Maier, R. G. Hennig, U. Wiesner, *Angew. Chem., Int. Ed.* **2011**, *50*, 11985.
[215] W. J. Chen, B. Hou, Z. Q. Zhang, J. B. Pendry, C. T. Chan, *Nat. Commun.* **2018**, *9*, 1.
[216] M. O'Keeffe, M. A. Peskov, S. J. Ramsden, O. M. Yaghi, *Acc. Chem. Res.* **2008**, *41*, 1782.
[217] M. W. Matsen, F. S. Bates, *Macromolecules* **1996**, *29*, 1091.
[218] C.-H. Lin, T. Higuchi, H.-L. Chen, J.-C. Tsai, H. Jinnai, T. Hashimoto, *Macromolecules* **2018**, *51*, 4049.
[219] A. C. Finnefrock, R. Ulrich, G. E. S. Toombes, S. M. Gruner, U. Wiesner, *J. Am. Chem. Soc.* **2003**, *125*, 13084.
[220] L. Ferrari, C. Wu, D. Lepage, X. Zhang, Z. Liu, *Prog. Quantum Electron.* **2015**, *40*, 1.
[221] A. Poddubny, I. Iorsh, P. Belov, Y. Kivshar, *Nat. Photonics* **2013**, *7*, 948.
[222] I. I. Smolyaninov, V. N. Smolyaninova, *Solid State Electron.* **2017**, *136*, 102.
[223] P. Shekhar, J. Atkinson, Z. Jacob, *Nano Converg.* **2014**, *1*, 14.
[224] P. A. Belov, *Microwave Opt. Technol. Lett.* **2003**, *37*, 259.
[225] D. R. Smith, D. Schurig, *Phys. Rev. Lett.* **2003**, *90*, 077405.
[226] X. Wang, K. Ehrhardt, C. Tallet, M. Warenghem, A. Baron, A. Aradian, M. Kildemo, V. Ponsinet, *Opt. Laser Technol.* **2017**, *88*, 85.
[227] J. Yao, Z. Liu, Y. Liu, Y. Wang, C. Sun, G. Bartal, A. M. Stacy, X. Zhang, *Science* **2008**, *321*, 930.
[228] S. Bang, S. So, J. Rho, *Sci. Rep.* **2019**, *9*, 1.
[229] E. E. Narimanov, V. M. Shalaev, *Nature* **2007**, *447*, 266.
[230] Y. Guo, C. L. Cortes, S. Molesky, Z. Jacob, *Appl. Phys. Lett.* **2012**, *101*, 131106.
[231] C. L. Cortes, W. Newman, S. Molesky, Z. Jacob, *J. Opt.* **2012**, *14*, 063001.
[232] S. M. Rytov, *J. Exper. Theor. Phys. USSR* **1956**, *2*, 605.
[233] A. L. Liberman-Martin, C. K. Chu, R. H. Grubbs, *Macromol. Rapid Commun.* **2017**, *38*, 1700058.
[234] H. Fudouzi, *Sci. Technol. Adv. Mater.* **2011**, *12*, 064704.

[235] S. P. Samant, C. A. Grabowski, K. Kisslinger, K. G. Yager, G. Yuan, S. K. Satija, M. F. Durstock, D. Raghavan, A. Karim, *ACS Appl. Mater. Interfaces* **2016**, *8*, 7966.
[236] T. W. H. Oates, H. Wormeester, H. Arwin, *Prog. Surf. Sci.* **2011**, *86*, 328.
[237] J. Toudert, *Nanotechnol. Rev.* **2014**, *3*, 223.
[238] C. L. Holloway, E. F. Kuester, J. A. Gordon, J. O'Hara, J. Booth, D. R. Smith, *IEEE Antennas Propag. Mag.* **2012**, *54*, 10.
[239] J. C. M. Garnett, *Philos. Trans. R. Soc., A* **1904**, *203*, 385.
[240] A. Heilmann, *Polymer Films with Embedded Metal Nanoparticles*, Springer, Berlin **2003**, pp. 149–197.
[241] G. Bánhegyi, *Colloid Polym. Sci.* **1986**, *264*, 1030.
[242] D. Bedeaux, J. Vlieger, *Optical Properties of Surfaces*, Imperial College Press, London **2004**.
[243] A. Alvarez-Fernandez, G. Fleury, V. Ponsinet, P. M. Walmsness, M. Kildemo, *J. Vac. Sci. Technol. B* **2020**, *38*, 013601.
[244] S. K. Patil, M. Y. Koledintseva, R. W. Schwartz, W. Huebner, *J. Appl. Phys.* **2008**, *104*, 074108.
[245] B. A. Belyaev, V. V. Tyurnev, *J. Exp. Theor. Phys.* **2018**, *127*, 608.
[246] C. S. T. Laicer, T. Q. Chastek, T. P. Lodge, T. A. Taton, *Macromolecules* **2005**, *38*, 9749.
[247] C.-T. Lo, Y.-C. Chang, S.-C. Wu, C.-L. Lee, *Colloids Surf., A* **2010**, *368*, 6.
[248] J. J. Chiu, B. J. Kim, G.-R. Yi, J. Bang, E. J. Kramer, D. J. Pine, *Macromolecules* **2007**, *40*, 3361.
[249] P. A. Mistark, S. Park, S. E. Yalcin, D. H. Lee, O. Yavuzcetin, M. T. Tuominen, T. P. Russell, M. Achermann, *ACS Nano* **2009**, *3*, 3987.
[250] L. Malassis, P. Massé, M. Tréguer-Delapierre, S. Mornet, P. Weisbecker, P. Barois, C. R. Simovski, V. G. Kravets, A. N. Grigorenko, *Adv. Mater.* **2014**, *26*, 324.
[251] J. Toudert, X. Wang, C. Tallet, P. Barois, A. Aradian, V. Ponsinet, *ACS Photonics* **2015**, *2*, 1443.
[252] V. G. Kravets, F. Schedin, R. Jalil, L. Britnell, R. V. Gorbachev, D. Ansell, B. Thackray, K. S. Novoselov, A. K. Geim, A. V. Kabashin, A. N. Grigorenko, *Nat. Mater.* **2013**, *12*, 304.
[253] H. Kang, S. Kim, S. Il Yoo, B. Sohn, *Adv. Mater. Interfaces* **2019**, *6*, 1901257.
[254] Z. Liu, H. Huang, T. He, *Small* **2013**, *9*, 505.
[255] F. Lai, T. Borca-Tasciuc, J. Plawsky, *Nanotechnology* **2015**, *26*, 055301.
[256] D. Solis, A. Paul, J. Olson, L. S. Slaughter, P. Swanglap, W.-S. Chang, S. Link, *Nano Lett.* **2013**, *13*, 4779.
[257] S. Kawata, A. Ono, P. Verma, *Nat. Photonics* **2008**, *2*, 438.
[258] V. M. Agranovich, V. Ginzburg, *Crystal Optics with Spatial Dispersion, and Excitons, Springer Series in Solid-State Sciences*, Vol. *42*, Springer, London **1984**, pp. 136–270.
[259] X. Wei, H. Shi, X. Dong, Y. Lu, C. Du, *Appl. Phys. Lett.* **2010**, *97*, 011904.
[260] H. L. Leertouwer, B. D. Wilts, D. G. Stavenga, *Opt. Express* **2011**, *19*, 24061.
[261] J. Zhang, K. F. MacDonald, N. I. Zheludev, *Light Sci. Appl.* **2012**, *1*, e18.
[262] H. Hulkkonen, A. Sah, T. Niemi, *ACS Appl. Mater. Interfaces* **2018**, *10*, 42941.
[263] C. Hägglund, G. Zeltzer, R. Ruiz, I. Thomann, H. B. R. Lee, M. L. Brongersma, S. F. Bent, *Nano Lett.* **2013**, *13*, 3352.
[264] P. Mokarian-Tabari, R. Senthamaraikannan, C. Glynn, T. W. Collins, C. Cummins, D. Nugent, C. O'Dwyer, M. A. Morris, *Nano Lett.* **2017**, *17*, 2973.
[265] B. Päivänranta, P. K. Sahoo, E. Tocce, V. Auzelyte, Y. Ekinci, H. H. Solak, C. C. Liu, K. O. Stuen, P. F. Nealey, C. David, *ACS Nano* **2011**, *5*, 1860.
[266] A. Rahman, A. Ashraf, H. Xin, X. Tong, P. Sutter, M. D. Eisaman, C. T. Black, *Nat. Commun.* **2015**, *6*, 5963.
[267] X. Zhang, A. B. Sushkov, C. J. Metting, S. Fackler, H. D. Drew, R. M. Briber, *Plasma Process. Polym.* **2012**, *9*, 968.
[268] J. Langer, D. Jimenez de Aberasturi, J. Aizpurua, R. A. Alvarez-Puebla, B. Auguié, J. J. Baumberg, G. C. Bazan, S. E. J. Bell, A. Boisen, A. G. Brolo, J. Choo, D. Cialla-May, V. Deckert, L. Fabris, K. Faulds, F. J. García de Abajo, R. Goodacre, D. Graham, A. J. Haes, C. L. Haynes, C. Huck, T. Itoh, M. Käll, J. Kneipp, N. A. Kotov, H. Kuang, E. C. Le Ru, H. K. Lee, J.-F. Li, X. Y. Ling, S. A. Maier, T. Mayerhöfer, M. Moskovits, K. Murakoshi, J.-M. Nam, S. Nie, Y. Ozaki, I. Pastoriza-Santos, J. Perez-Juste, J. Popp, A. Pucci, S. Reich, B. Ren, G. C. Schatz, T. Shegai, S. Schlücker, L.-L. Tay, K. G. Thomas, Z.-Q. Tian, R. P. Van Duyne, T. Vo-Dinh, Y. Wang, K. A. Willets, C. Xu, H. Xu, Y. Xu, Y. S. Yamamoto, B. Zhao, L. M. Liz-Marzán, *ACS Nano* **2020**, *14*, 28.
[269] Y. Wang, M. Becker, L. Wang, J. Liu, R. Scholz, J. Peng, U. Gösele, S. Christiansen, D. H. Kim, M. Steinhart, *Nano Lett.* **2009**, *9*, 2384.
[270] G. E. Akinoglu, S. H. Mir, R. Gatensby, G. Rydzek, P. Mokarian-Tabari, *ACS Appl. Mater. Interfaces* **2020**, *12*, 23410.
[271] Y. Shen, Y. Liu, W. Wang, F. Xu, C. Yan, J. Zhang, J. Wang, A. Yuan, *RSC Adv.* **2016**, *6*, 38716.
[272] Y. Chen, S. Xiong, *Int. J. Extrem. Manuf.* **2020**, *2*, 032006.
[273] H. M. Jin, J. Y. Kim, M. Heo, S. J. Jeong, B. H. Kim, S. K. Cha, K. H. Han, J. H. Kim, G. G. Yang, J. Shin, S. O. Kim, *ACS Appl. Mater. Interfaces* **2018**, *10*, 44660.
[274] C. J. Powell, J. B. Swan, *Phys. Rev.* **1959**, *115*, 869.
[275] S. V. Boriskina, H. Ghasemi, G. Chen, *Mater. Today* **2013**, *16*, 375.
[276] R. H. Siddique, J. Mertens, H. Hölscher, S. Vignolini, *Light Sci. Appl.* **2017**, *6*, e17015.
[277] N. Dean, *Nat. Nanotechnol.* **2015**, *10*, 15.
[278] E. Højlund-Nielsen, J. Clausen, T. Mäkela, L. H. Thamdrup, M. Zalkovskij, T. Nielsen, N. Li Pira, J. Ahopelto, N. A. Mortensen, A. Kristensen, *Adv. Mater. Technol.* **2016**, *1*, 1600054.
[279] B. Guo, L. Jiang, Y. Hua, N. Zhan, J. Jia, K. Chu, Y. Lu, *ACS Omega* **2019**, *4*, 7467.
[280] Z. Wu, Y. Zheng, *Adv. Opt. Mater.* **2018**, *6*, 1701057.
[281] C. Cummins, G. Pino, D. Mantione, G. Fleury, *Mol. Syst. Des. Eng.* **2020**, *5*, 1642.
[282] M. D. Rodwogin, A. Baruth, E. A. Jackson, C. Leighton, M. A. Hillmyer, *ACS Appl. Mater. Interfaces* **2012**, *4*, 3550.
[283] A. Alvarez-Fernandez, F. Valdes-Vango, J. I. Martín, M. Vélez, C. Quirós, D. Hermida-Merino, G. Portale, J. M. Alameda, F. J. García Alonso, *Polym. Int.* **2019**, *68*, 1914.
[284] A. Álvarez-Fernández, F. Valdés-Bango, R. Losada-Ambrinos, J. I. Martín, M. Vélez, J. M. Alameda, F. J. García Alonso, *Polym. Int.* **2018**, *67*, 393.
[285] K. Aissou, A. Nunns, I. Manners, C. A. Ross, *Small* **2013**, *9*, 4077.
[286] S. Antoine, K. Aissou, M. Mumtaz, G. Pécastaings, T. Buffeteau, G. Fleury, G. Hadziioannou, *Macromol. Rapid Commun.* **2019**, *40*, 1800860.
[287] N. Demazy, C. Cummins, K. Aissou, G. Fleury, *Adv. Mater. Interfaces* **2020**, *7*, 1901747.
[288] Y. Zhou, I. I. Kravchenko, H. Wang, H. Zheng, G. Gu, J. Valentine, *Light Sci. Appl.* **2019**, *8*, 1.
[289] A. Rahman, P. W. Majewski, G. Doerk, C. T. Black, K. G. Yager, *Nat. Commun.* **2016**, *7*, 13988.
[290] P. W. Majewski, A. Rahman, C. T. Black, K. G. Yager, *Nat. Commun.* **2015**, *6*, 7448.
[291] A. Alvarez-Fernandez, F. Nallet, P. Fontaine, C. Cummins, G. Hadziioannou, P. Barois, G. Fleury, V. Ponsinet, *RSC Adv.* **2020**, *10*, 41088.
[292] C. Jin, B. C. Olsen, E. J. Luber, J. M. Buriak, *ACS Nano* **2017**, *11*, 3237.
[293] Z. Wu, Y. Zheng, *Adv. Opt. Mater.* **2018**, *6*, 1701057.
[294] C. Jin, B. C. Olsen, E. J. Luber, J. M. Buriak, *Chem. Mater.* **2017**, *29*, 176.

[295] R. Lundy, S. P. Flynn, C. Cummins, S. M. Kelleher, M. N. Collins, E. Dalton, S. Daniels, M. A. Morris, R. Enright, *Phys. Chem. Chem. Phys.* **2017**, *19*, 2805.
[296] C. Cummins, A. Alvarez-Fernandez, A. Bentaleb, G. Hadziioannou, V. Ponsinet, G. Fleury, *Langmuir* **2020**, *36*, 13872.
[297] A. Subramanian, N. Tiwale, G. Doerk, K. Kisslinger, C. Y. Nam, *ACS Appl. Mater. Interfaces* **2020**, *12*, 1444.
[298] D. Berman, S. Guha, B. Lee, J. W. Elam, S. B. Darling, E. V. Shevchenko, *ACS Nano* **2017**, *11*, 2521.
[299] X. Chen, P. R. Delgadillo, Z. Jiang, G. S. W. Craig, R. Gronheid, P. F. Nealey, *Macromolecules* **2019**, *52*, 7798.
[300] T. Segal-Peretz, J. Ren, S. Xiong, G. Khaira, A. Bowen, L. E. Ocola, R. Divan, M. Doxastakis, N. J. Ferrier, J. De Pablo, P. F. Nealey, *ACS Nano* **2017**, *11*, 1307.

Alberto Alvarez Fernandez received his Ph.D. at the University of Bordeaux (France) in 2018, working on the development of new plasmonic metasurfaces using block copolymers, with Dr. Virginie Ponsinet and Dr. Guillaume Fleury. Thereafter, he has joined the Adaptive & Responsive Nanomaterials group at the University College London (UK) as a postdoctoral researcher. His research interests include the development of complex plasmonic nanostructures and mesoporous architectures based on block copolymer self-assembly for sensing and optical applications.

Cian Cummins is currently a postdoctoral researcher at University of Bordeaux studying block copolymer thin films for photonic applications with Dr. Guillaume Fleury and Dr. Virginie Ponsinet. His primary research interests focus on developing new methods for modifying nanoscale polymer templates for semiconductor, sensing, and energy applications. He completed his Ph.D. on inorganic block copolymer nanolithography in 2015 (University College Cork, Ireland) with Prof. Mick Morris.

Matthias Saba received a Ph.D. degree in Physics in 2015 from the University of Erlangen-Nuremberg (Germany) for his work on chiral biomimetic photonic crystals. He joined the Condensed Matter Theory Group at Imperial College London from 2015 to 2019, where he studied 3D photonic topological materials and metamaterials. His current research interest as a group leader in the Soft Matter Physics Group at the Adolphe Merkle Institute (Switzerland) focusses on the theory of double-network and self-assembled optical metamaterials.